energies

MDPI

Article

Numerical Analysis of Two-Stage Turbine System for Multicylinder Engine under Pulse Flow Conditions with High Pressure-Ratio Turbine Rotor

Dariusz Kozak * and Paweł Mazuro

Department of Aircraft Engines, Faculty of Power and Aeronautical Engineering, Institute of Heat Engineering, Warsaw University of Technology, 00-665 Warsaw, Poland

* Correspondence: dariusz.kozak.dokt@pw.edu.pl; Tel.: +48-509-679-182

Abstract: Internal combustion engine (ICE) exhaust gases provide a high amount of energy which is partially lost to the environment. Such energy can be recovered with a turbocharger turbine or other after-treatment device. As the engine exhaust flow varies not only with the engine load but also with the opening and closing of the exhaust valves, a proper matching between the engine and the turbine should be established to maximize the recovery of waste energy. That is why a twin-scroll or dual turbocharging system is implemented, especially in multi-cylinder engines. Such systems require a very complex pipeline to eliminate the interference of the exhaust pulses between the adjacent cylinder ignitions. In this study, the two-stage, multi-channel turbine system was investigated for two different rotor geometries: the old, high-performance rotor A and the smaller but more modern rotor B, which was scaled to match rotor A. Both geometries were compared at three different turbine speeds and variable turbine geometry (VTG) vane positions. It was found that the two-stage turbine system with rotor B geometry provided an 8% higher total efficiency than rotor A due to the lower flow losses within the rotor passage.

Keywords: CFD; radial turbine; exhaust system; VTG; efficiency; internal combustion engine; unsteady flow; turbocharging

Citation: Kozak, D.; Mazuro, P. Numerical Analysis of Two-Stage Turbine System for Multicylinder Engine under Pulse Flow Conditions with High Pressure-Ratio Turbine Rotor. *Energies* **2023**, *16*, 751. https://doi.org/10.3390/en16020751

Academic Editor: Roberto Finesso

Received: 30 November 2022
Revised: 21 December 2022
Accepted: 4 January 2023
Published: 9 January 2023

1. Introduction

The modern ICE is required to be efficient and economical; thus, the engine manufacturers are forced to implement reliable and complex systems to enhance power and reduce fuel consumption. Additionally, emission regulations place other constraints on engine design. Implementing turbochargers is one of the key trends to increase engine efficiency and decrease fuel consumption. However, the main problem with the turbocharger implementation is matching the turbocharger to the engine performance. The ICE operates under different loads and speeds; thus, the turbocharger should be efficient at the engine's low- and high-load conditions. Utilizing a turbocharger with variable turbine geometry (VTG) increased engine efficiency at low and high loads due to the variable nozzle vanes at the inlet to the rotor. However, such a system is very complex and requires a specially-designed control system.

The ICE operates under constantly changing conditions. Thus, the exhaust mass-flow rate and pressure cannot be treated as constant [1]. Such a phenomenon is critical in multicylinder engines where exhaust pulsations occur with higher frequency [2–4]. Thus, the exhaust pulsation should be carefully examined based on the cycle-averaged exhaust heat energy [5].

Most manufacturers determine turbocharger performance based on steady-state conditions mainly because of the simplicity of the experimental test stand. The investigation of turbocharger performance under pulse-flow conditions requires a complex test stand that requires a device to simulate the pulse-like flow of the exhaust gases. Some experimental

tests are conducted under steady-state conditions [6,7]. Such tests are performed mainly for twin-entry turbines. The test stand is equipped with a bypass valve which provides different admission of the exhaust mass flow rate for each turbine inlet pipe. The simulated engine exhaust conditions are mostly simplified with the compressed, pre-heated air as a working fluid. The specially-designed pulse generator simulates the pulse flow of the exhaust gases with different frequencies. The transient experimental test stand requires an eddy current dynamometer which provides the transient response of the turbine or turbocharger [8]. The specially-designed rotating plates also provide pulsating behavior of the hot gases. The main difficulty of the experimental tests lies in estimating the turbine output power, due to problems with temperature measurement. Thus, the turbine output power is mainly measured based on the torque of the eddy dynamometer or the compressor wheel. One of the main findings of the experimental test was that the turbine efficiency plot under pulse flow presented a closed-loop enclosing the steady-state line [9]. Thus, the turbine performance under pulse conditions dramatically deviates from the steady-state conditions.

The numerical software provides a faster and cheaper way to perform a simplified simulation of a turbine turbocharger model. Researchers widely use turbine simulations at the early stage of turbocharger design. The one-dimensional (1-D) computational fluid dynamics (CFD) software calculates a simplified turbine model relatively quickly. In such models, the volute and turbine are represented as divergent ducts with different lengths [10]. Such a model is exceptionally efficient at pulse flow conditions due to its reduced calculation time. Such a model does not include tip clearance loss or bearing losses. The numerical model enables an investigation of the pulse frequency and amplitude influence at different turbine speeds [11]. The 1-D turbine model is based on the one-dimensional momentum equation and is treated as quasi-steady due to its small size [12,13].

More detailed analysis can be performed with the three-dimensional (3-D) CFD simulations. Such simulations not only provide investigation of the complete rotor geometry but also allow us to investigate the flow structure within the rotor passage. The investigation of flow structures allows for judging the source of efficiency losses at a certain turbine working point. However, the main drawbacks of 3-D simulations are the long computational time and the demanding computational memory resources. Thus, most of the computational packages provide simplified simulation methods of the turbine rotor. The turbine rotor can be simulated as a periodic, single-flow passage with a specific pitch ratio between the nozzle vanes. The steady-state simulations are mostly related to the different flow admissions for the double-entry turbine [14]. In such calculations, the exhaust mass-flow rate is constant but varies for each inlet duct. Such a model enables investigation of the full-admission conditions, where the mass-flow rate is the same in each inlet duct or partial-admission. The entropy loss model measures losses in each numerical domain [15]. The highest losses for the double-entry turbine are observed at full-admission conditions due to the high mixing losses at the turbine outlet. The transient 3-D simulations provide information to compare the timescale within a pulsed-flow turbocharger turbine in terms of Strouhal number (St) [16,17]. The St indicates the time ratio needed for a particle to travel the domain length to the time associated with the considered disturbance. The unsteadiness can be neglected at a relatively low St ($St < 1$). However, the unsteadiness cannot be neglected at high St values ($St > 1$). At $St = 1$, both unsteady and steady disturbances are important. Thus, the volute provided a high St number due to its length. However, the nozzle provided a low St number; thus, its unsteadiness can be neglected. The rotor domain can only be treated as partially unsteady due to rotor passage length. The 3-D numerical simulations provide insight into the flow structure inside the twin-entry turbocharger domains [18]. The secondary-flow structures are more frequently observed at the volute due to the increased unsteadiness [19]. However, the turbine performance increases with the St number, which indicates that the twin-entry turbine works efficiently at pulse flow conditions. The 3-D model enables the investigation of the incidence angle changes at different pulse frequencies and amplitude values [20,21]. Such incidence angle

significantly affects the turbine performance as the pulse frequency changes. The increase in the pulse frequency leads to a lower variation of the incidence angle, resulting in improved turbine performance.

The abovementioned articles provide insight into the research of the turbocharger turbine under pulse flow conditions. The limited number of research papers regarding turbine simulations under pulse flow conditions suggests that such simulations are very demanding and require accurate boundary conditions based on actual driving conditions. This paper presents the research results of the unsteady, 3-D numerical simulation of the unique two-stage turbine system. The connection of the multi-channel rotor inlet and the two-stage system makes this system unique. So far, such features have been investigated separately [22,23]. Thus, such numerical simulations are exciting regarding total efficiency and flow structures. The model was simulated with two rotor geometries: A and B. The rotor A geometry is the older generation rotor manufactured for high-performance sports cars. Although significantly smaller, the real-scale, state-of-the-art rotor B provided only a slightly lower performance than rotor A; thus, rotor B was scaled to match the rotor A dimensions to make a fair comparison.

2. Rotor A and Rotor B

The research of the two-stage turbine model was conducted for two different geometries of the turbine wheel, as shown in Figure 1.

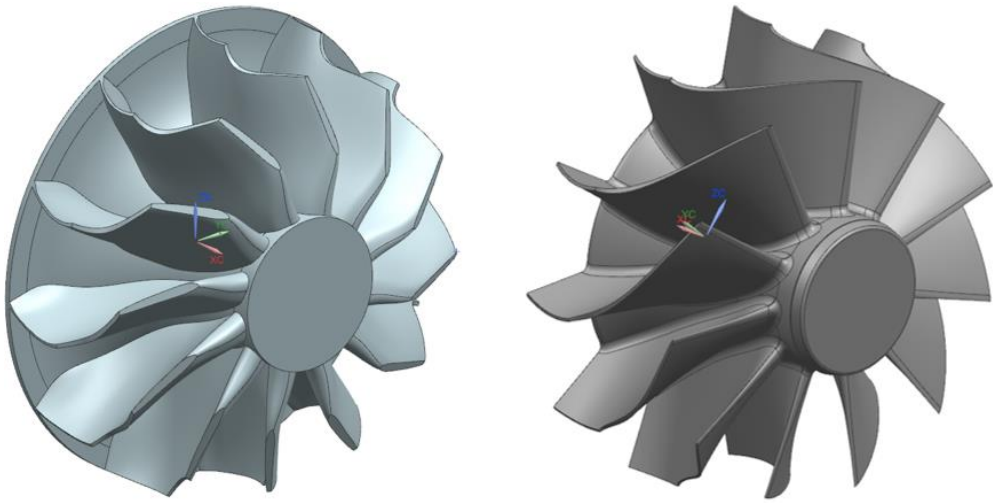

Figure 1. The geometries of (**a**) Rotor A—older version of turbine wheel and (**b**) Rotor B—latest version of turbine wheel (scaled to match the diameter of the Rotor A).

Figure 1 shows that rotor A consists of 12 blades, while rotor B consists of 11 blades. Rotor B is the latest generation of the turbine wheel. The performance of both wheels can be seen in Figure 2 and Table 1.

Figure 2 shows the performance of both rotor wheels. As can be seen, rotor A is larger than rotor B. The inlet diameter of rotor A is 40% larger than the inlet diameter of rotor B. On the other hand, rotor B operates at higher pressure ratio values. It can also be seen that rotor B had fewer blades than rotor A. Due to the smaller diameter of rotor B, its flow capabilities are lower than that of rotor A. The maximal mass-flow rate of rotor B is 1.15 kg/s, while the maximal flow of rotor A is 1.45 kg/s. However, such a difference is relatively small when considering a notable difference in diameter.

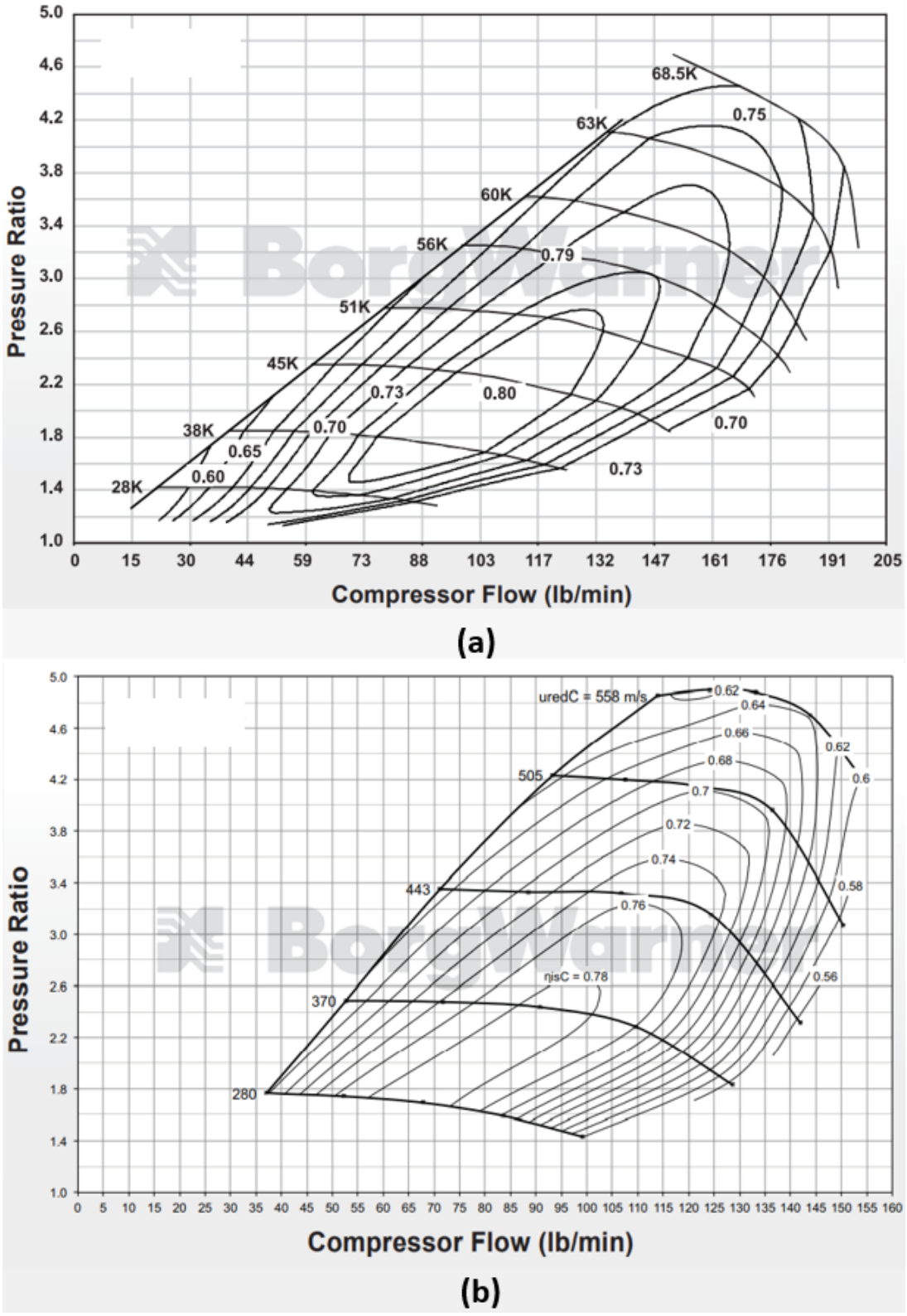

Figure 2. The performance data of (**a**) rotor A and (**b**) rotor B [24].

Table 1. The performance data of rotors A and B.

Rotor A	
Inlet diameter (m)	0.140
Outlet diameter (m)	0.125
Number of blades	12
Maximal rotor speed (rpm)	68,500
Maximal pressure ratio (-)	4.4
Maximal mass flow rate (kg/s)	1.45
Rotor B	
Inlet diameter (m)	0.11
Outlet diameter (m)	0.10
Number of blades	11
Maximal rotor speed (rpm)	97,000
Maximal pressure ratio (-)	4.8
Maximal mass flow rate (kg/s)	1.15

In order to compare both rotors, rotor B was scaled up to match the dimensions of rotor A. Such an approach allowed us to perform a fair comparison of both rotors. Moreover, as can be seen in Figure 2 and Table 1, the difference in maximal mass-flow rate between both rotors is relatively tiny compared to the large difference in inlet diameter. Thus, the performance of scaled rotor B might equal or even exceed the performance of rotor A.

A more detailed comparison of scaled rotor B and rotor A can be undertaken by comparing angular changes of the blades. For this purpose, the theta θ and β angles were considered. The beta angle β indicates the blade deviation from the longitudinal axis of the rotor, while theta angle θ indicates blade deviation from the axis perpendicular to the longitudinal axis. The comparison of both parameters can be seen in Figure 3.

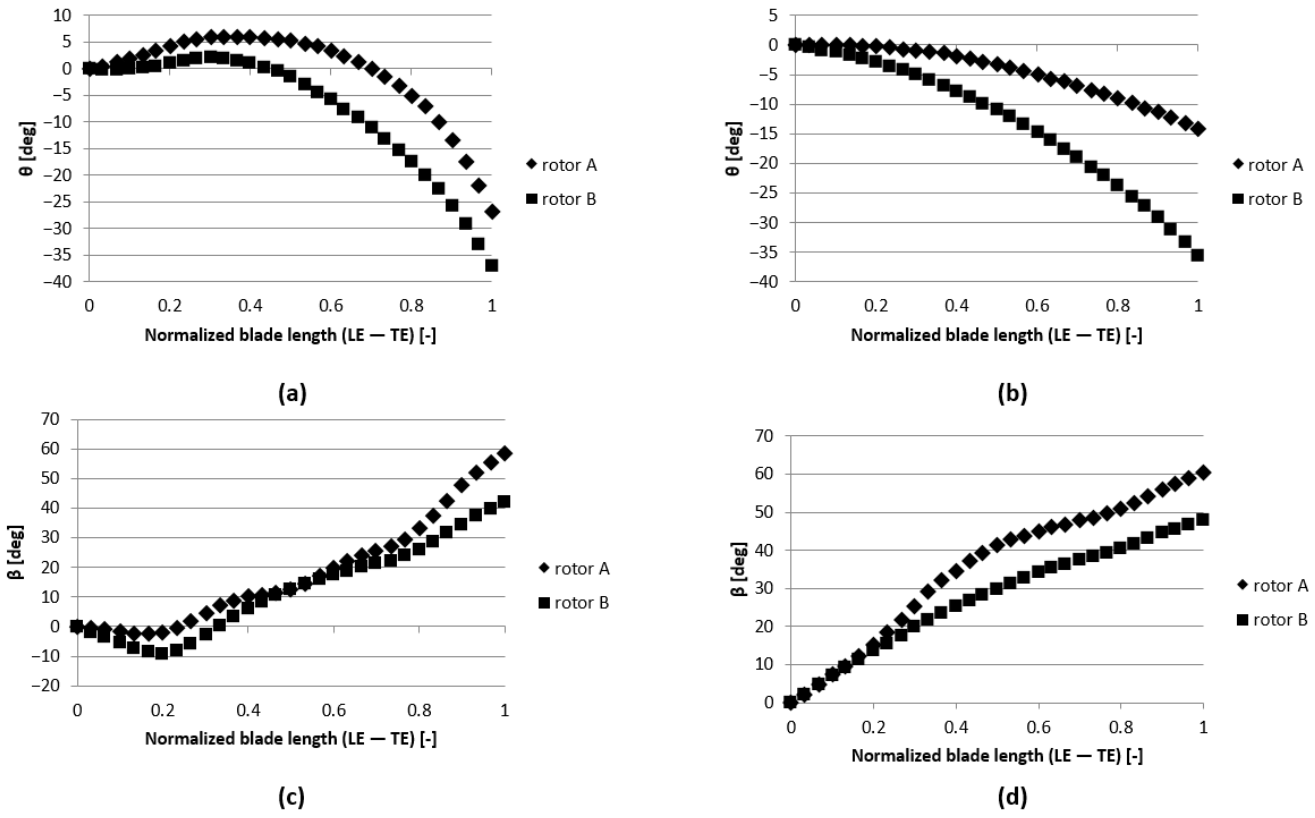

Figure 3. Angular comparison of rotors A and B: (**a**) theta angle at hub, (**b**) theta angle at shroud, (**c**) beta angle at hub and (**d**) beta angle at shroud.

Figure 3 shows the changes in theta and beta angles at the hub and shroud along the blade length from the leading edge (LE) to the trailing edge (TE). As can be seen, the highest deviation between rotors A and B can be observed at the trailing edge. The negative sign indicates that the blade deviates opposite to the rotation of the rotor. At the hub, the theta angle difference between rotors reaches 10° at the TE, while the beta angle difference reaches 17° at the TE. The stress requirements limit such differences. Higher difference values can be observed at the shroud, where the geometry is not limited by the mechanical stress but by the flow losses. The theta angle difference is significant at the shroud compared to the beta angle. The difference in theta angle at the TE reaches 21°, which indicates that the blades of rotor B have a higher deviation in the opposite direction to the rotation. The beta angle difference reaches 12.5° at the TE, which indicates that the blades of rotor B are less twisted than the blades of rotor A. This might lead to a smaller flow circulation at the outlet from rotor B.

3. Radial Inflow Turbine

The performance of the radial inflow turbine greatly depends on the gas thermodynamic parameters at the rotor inlet. Most radial turbines operate under a high pressure difference between the rotor inlet and outlet. Thus, such pressure difference is defined as the pressure-ratio (PR) and expressed as [25]:

$$\pi_T = \frac{p_0^*}{p_2} \tag{1}$$

where, the π_T stands as the PR and the indexes "0" and "2" define the rotor inlet and outlet.

The above expression is often used to define the desired drop of the isentropic enthalpy Δh_{iz} when the inlet temperature T_0^* is known:

$$\Delta h_{iz} = \frac{k'}{k'-1} R' T_0^* [1 - \frac{1}{\pi_T^{\frac{k'-1}{k'}}}] \tag{2}$$

where k' is the heat capacity ratio of exhaust gases and the R' is the gas constant of the exhaust gases.

For the nozzles turbine, the outlet temperature T_2 can be expressed as:

$$T_2 = T_0^* - \frac{w_2^2 - w_0^2}{2\frac{k'}{k'-1}R'} \tag{3}$$

For the turbine with nozzle vanes, the temperature T_2 can be obtained as:

$$T_2 = T_1 - \frac{w_2^2 - w_1^2}{2\frac{k'}{k'-1}R'} \tag{4}$$

where T_1 is the temperature behind the nozzle vanes:

$$T_1 = T_0^* - \frac{c_1^2}{2\frac{k'}{k'-1}R'} \tag{5}$$

The velocities w_2 and w_0 indicate the relative velocity at the outlet and inlet to the rotor. The c_1 indicates the velocity behind the nozzle vanes which can be obtained from:

$$c_1 = \frac{u}{\left(\frac{u}{c_1}\right)_{opt}} \tag{6}$$

where $\left(\frac{u}{c_1}\right)_{opt}$ is the optimal ratio between the rotor linear velocity u and the rotor absolute velocity at the inlet c_1. For most of the cases, such optimal values range from 0.6 to 0.75 to achieve the maximal isentropic efficiency.

Those relative velocities w_2 and w_0 are calculated based on the triangle velocity formula:

$$w = c - u \tag{7}$$

Such formula concerns the inlet and outlet of the rotor and nozzle vane sections.

4. Numerical Domain

The 3-D, CFD calculations were performed with the use of the ANSYS Fluent software. Thus, the numerical code employed three governing equations [26]:

Continuity equation

$$\frac{\partial \rho}{\partial t} + \nabla(\rho U) = 0 \tag{8}$$

Momentum equations

$$\frac{\partial(\rho U)}{\partial t} + \nabla(\rho U \times U) = -\nabla p + \nabla \tau + S_M \tag{9}$$

Total energy equation

$$\frac{\partial(\rho h_{tot})}{\partial t} + \frac{\partial p}{\partial t} + \nabla(\rho U h_{tot}) = \nabla(\lambda \nabla T) + \nabla(U\tau) + US_M + S_E \tag{10}$$

The numerical model aims to recover as much energy from exhaust gases as possible. That is why the unique two-stage turbine system was designed and simulated to judge its efficiency for the six-cylinder, two-stroke, opposed-piston engine. The parameters of the engine are shown in Table 2 [27].

Table 2. The parameters of the six-cylinder, two-stroke, opposed-piston engine [27].

Engine Parameters	
Number of cylinders	6
Type	2-stroke
Rotational speed (rpm)	1500
Cylinder bore (mm)	115
Cylinder Stroke (mm)	195.2
Displacement (cm^3)	24,000
Crankshaft angle step (deg)	0.1

The central part of the numerical model was the two identical rotors that rotated at the same rotational speed; thus, they were placed on the same shaft. The numerical simulations were performed under the pulse-flow conditions. Such an approach allowed us to investigate the two-stage turbine system performance under the actual working condition of the engine. Most of the numerical simulations related to the research of the inflow turbines are focused on steady-state simulations. Such simulations are favorable in terms of computational expense. However, such simulations neglect the pressure wave interaction during the opening and closing of the exhaust valves. The authors consider the research results presented in this paper very attractive and worth discussing.

The numerical model consists of a uniquely-designed turbine inlet, the first-stage nozzle vane, a gap between the rotor and rotor hub, the first-stage rotor, the diffuser, the inter-stage pipes, the second-stage VTG vanes, the second-stage rotor, and the outlet. The cross-section of the model is shown in Figure 4 [27].

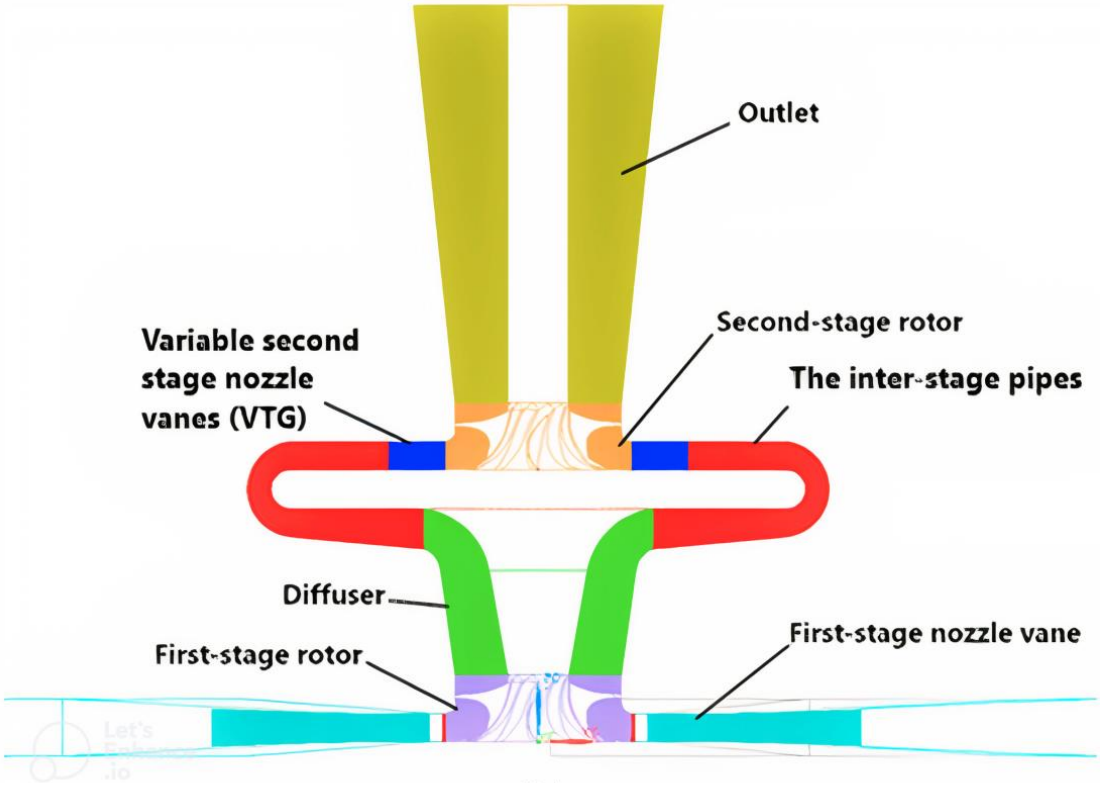

Figure 4. The cross-sectional view of the model [27].

The unique inlet separates the exhaust pulses from each cylinder. The inlet is made of six exhaust pipes equally placed along the circumference of the first-stage rotor. Each exhaust pipe connects each cylinder with the first-stage rotor to separate the exhaust pulses during the exhaust from the adjacent cylinders. The configuration of the inlet can be seen in Figure 5 [27].

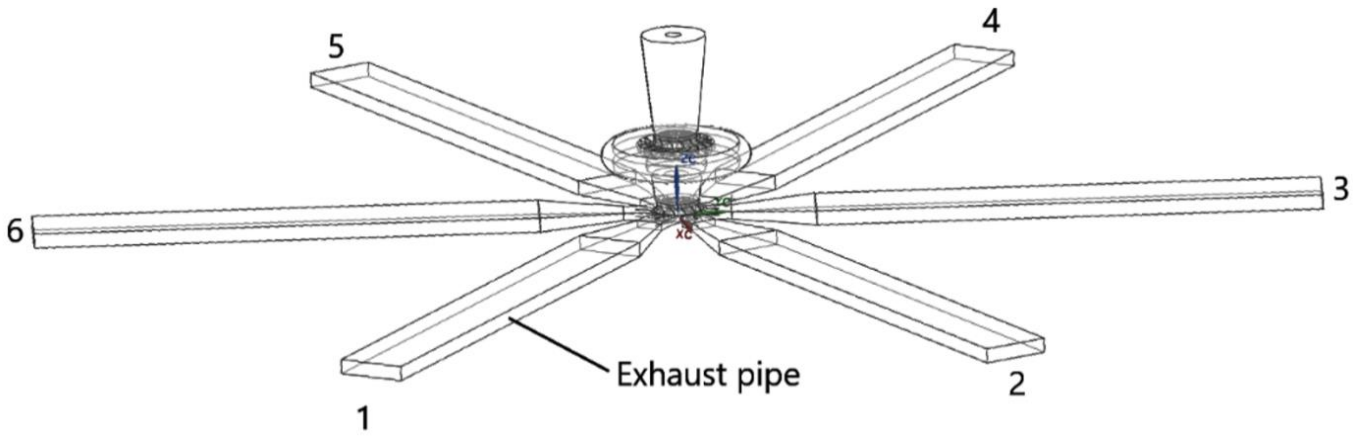

Figure 5. The configuration of the turbine inlet with the six exhaust pipes [27].

The first-stage nozzle vane comprised of a single vane positioned in the middle of the exhaust duct. The distance between the vane TE and rotor LE was set to 3 mm. The angle of the nozzle vane was set to 30°, based on the researcher's experience with previous models. It was found that such an angle provided a small amount of flow separation at the nozzle TE.

A rotor gap was modeled to simulate the gap between the tip of the first-stage rotor and the rotor hub. The gap height was set to 3 mm to capture the leakage between the adjacent exhaust pipes during the exhaust pulse. The captured losses allowed the authors

to investigate the effectiveness of the designed inlet. The first-stage nozzle vane and the rotor gap are shown in Figure 6.

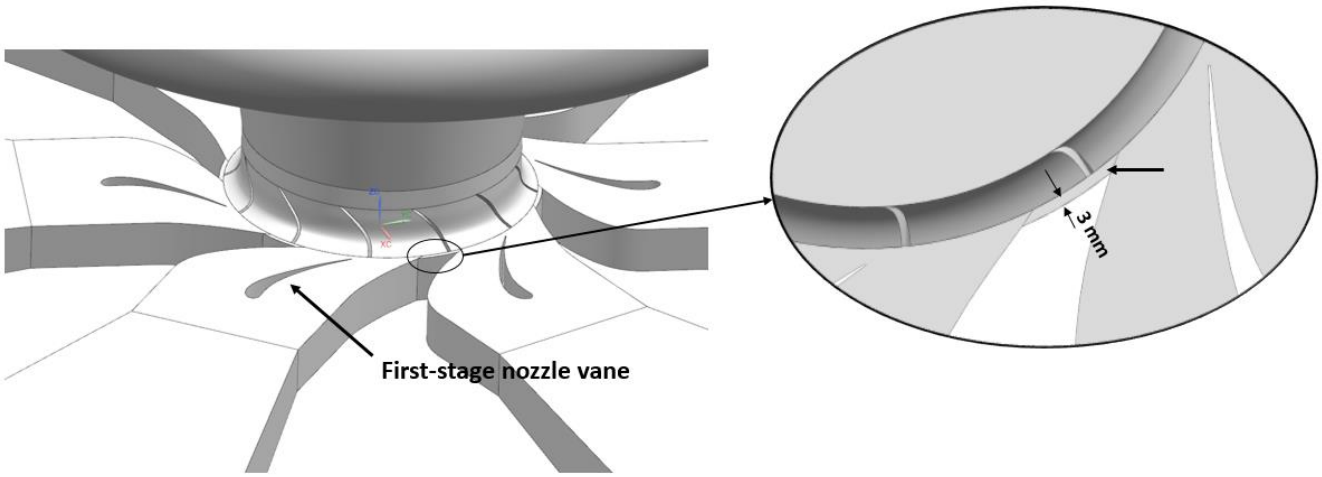

Figure 6. The first-stage nozzle vane and rotor gap.

The first-stage rotor model was created using the AKON smartSCAN 3D HE scanner. A total of 60 scans were made during the one revolution of the turntable. Figure 7 shows the scanning process of rotor A [27].

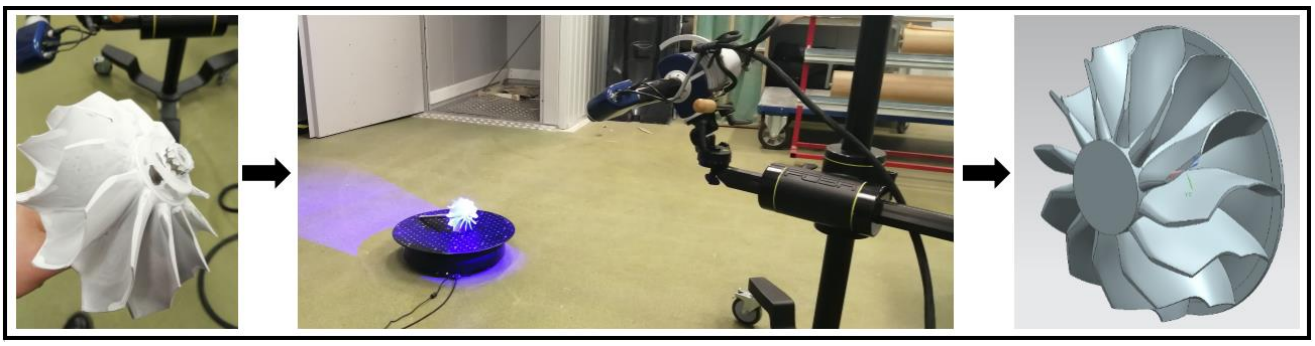

Figure 7. The scanning process of rotor A [27].

The diffuser and inter-stage pipes were iteratively modeled with the same approach as in the authors' previous work [27]. The primary purpose of the diffuser and the inter-stage pipes was to minimize the pressure losses between both stages.

The second-stage VTG vanes guided the exhaust gases to the second-stage rotor. The simulation was carried out at three different VTG vane positions to optimize the numerical model. The nozzle vanes were set at the specified angles: 20°, 30°, and 40°, which indicated the closed, medium, and fully-opened positions of the VTG vanes. The domain of the VTG vanes can be seen in Figure 8.

The second-stage rotor geometry was the same as the first-stage rotor. The second-stage rotor rotated at the same speed as the first-stage rotor.

The outlet domain was designed as an expanding cone whose length was set to six times the inlet diameter of the second-stage rotor. Such an approach was performed to avoid the backflow from the outlet.

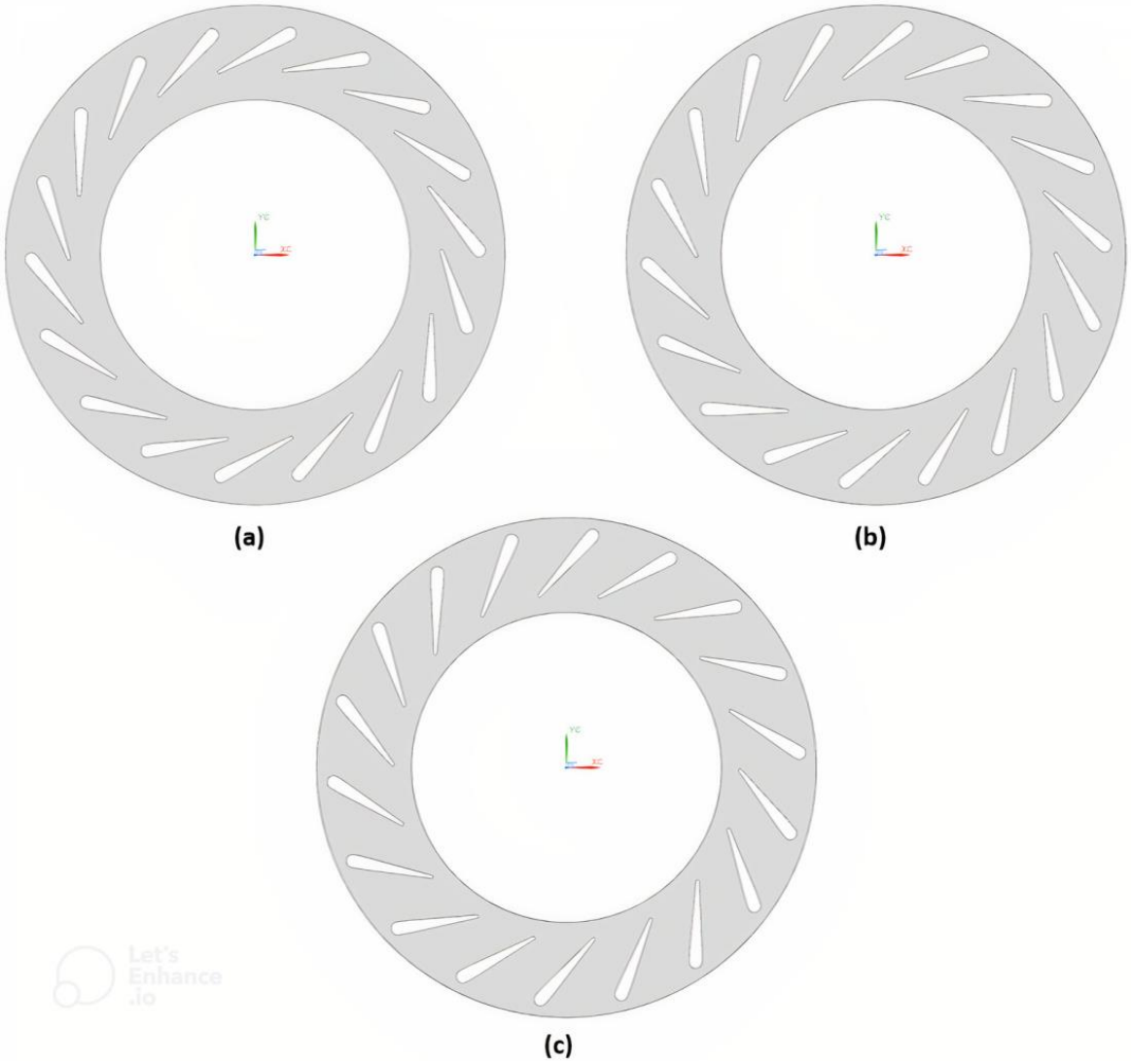

Figure 8. The position of the VTG vanes: (**a**) 20°, (**b**) 30° and (**c**) 40°.

4.1. Numerical Mesh

The numerical mesh was created with the ANSYS 2021 ICEM CFD software. The structural hexahedral mesh was created at the inlet domain, first-stage nozzle vanes domain, diffuser and inter-stage pipes domains, variable second-stage nozzle vanes domain, and outlet domain. However, the unstructured polyhedral mesh was created on the first-stage and second-stage rotor domains. This unstructured polyhedral mesh provides a lower number of numerical elements at the lower computational time and higher stability than the tetrahedral mesh [28]. Additionally, the whole rotational domain was simulated instead of a single passage. This decision was based on the authors' experience in previous simulations. Such an approach allowed us to simulate each passage simultaneously without adjusting the pitch ratio between the nozzle vanes and the single rotor passage. It was obvious that such simulations were very demanding regarding the computational time. However, transforming tetrahedral mesh into polyhedral significantly reduced the simulation time and numerical error. The numerical mesh can be seen in Figure 9.

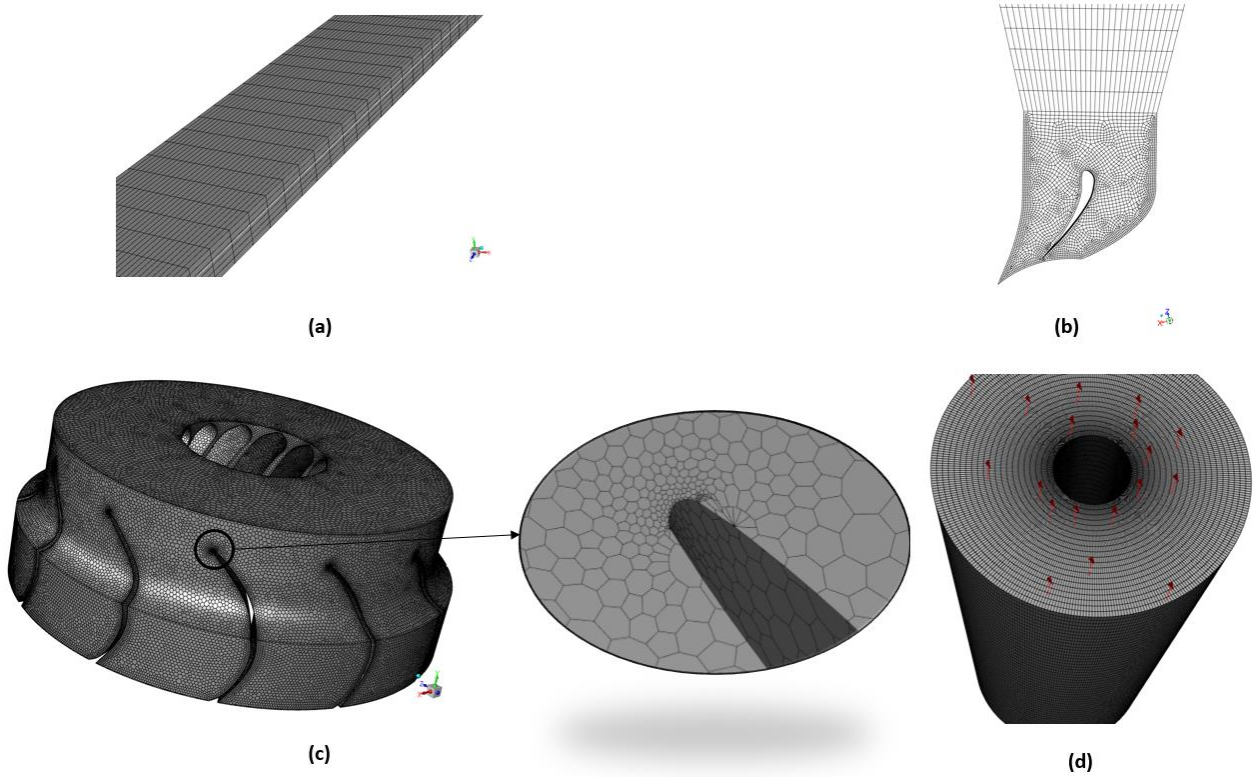

Figure 9. The numerical mesh of the model: (**a**) the inlet domain, (**b**) the first-stage nozzle vane domain, (**c**) the first- and second-stage rotor domain, (**d**) the outlet domain.

The VTG vanes were meshed separately according to the angular position of the vanes. The numerical mesh of the VTG vanes domain is shown in Figure 10.

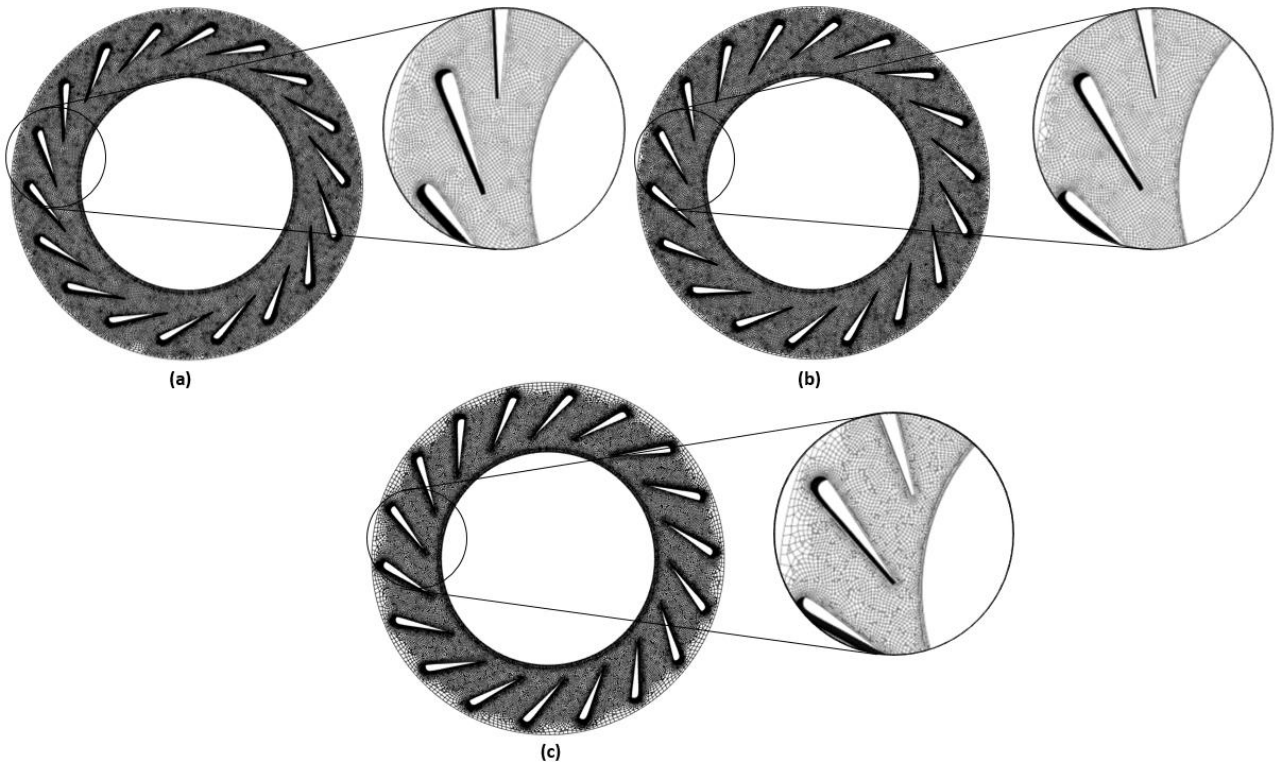

Figure 10. The numerical mesh of the VTG vanes domain at the angle (**a**) 20°, (**b**) 30°, (**c**) 40°.

4.2. Simulation Setup

The numerical model was simulated in the ANSYS Fluent software. The unsteady simulations were performed for the two geometries of the rotors, rotor A and rotor B, at three different rotational speeds: 40,000 rpm, 50,000 rpm, and 60,000 rpm. The different positions of the VTG vanes (20°, 30°, and 40°) were also investigated at each turbine speed. The simulated cases can be seen in Table 3. A relatively low time step was used to capture the unsteady changes in flow parameters between the steady and rotary domains. The authors set the time step value of 1.1×10^{-5} s. Thus, the blade angular changes per time step were 2.6°, 3.3°, and 4° for the turbine speed of 40,000 rpm, 50,000 rpm, and 60,000 rpm, respectively. Such time step was chosen to accurately predict the flow structures. It was found that the minor time step significantly increased the computational cost of the model without significant changes in the flow parameters. On the other hand, a higher time step generated a significant difference between the experimental and CFD data. Consequently, each pulse signal was discretized by approximately 2000 points. The Spalart-Allmaras (S-A) turbulence model was used for the simulation purposes [29]. Such a turbulence model was used based on the authors' experience with previous models. The S-A model is a single-equation turbulence model in which modified turbulence kinematic viscosity is linear in the near-wall region. This feature reduces the computational time. Such a model was widely used in turbomachinery simulations for unstructured mesh [30,31].

Table 3. Numerical cases for the simulated model.

Case	Turbine Speed *n* (rpm)	VTG Vane Positions (deg)
1	40,000	20
2		30
3		40
4	50,000	20
5		30
6		40
7	60,000	20
8		30
9		40

The transport equation of the S-A model was defined as [32]:

$$\frac{\partial}{\partial t}(\rho\check{\nu}) + \frac{\partial}{\partial x_i}(\rho\check{\nu}u_i) = G_\nu + \frac{1}{\sigma_{\check{\nu}}}\left[\frac{\partial}{\partial x_j}\left\{(\mu + \rho\check{\nu})\frac{\partial\check{\nu}}{\partial x_j}\right\} + C_{b2\rho}\left(\frac{\partial\check{\nu}}{\partial x_j}\right)^2\right] - Y_\nu + S_{\check{\nu}} \quad (11)$$

The turbulent viscosity is computed as:

$$\mu_t = \rho\check{\nu}f_{v1} \quad (12)$$

where:

$$f_{v1} = \frac{X^3}{X^3 - C_{v1}^3} \quad (13)$$

$$X \equiv \frac{\check{\nu}}{\nu} \quad (14)$$

Due to the unstructured mesh, the coupled pressure-velocity solver was used, providing stabilized calculations. Additionally, the second-order discretization scheme was used for pressure, density and momentum.

4.3. Boundary Conditions

The mass-flow inlet boundary condition was set at the inlet to each exhaust pipe and was obtained from the experimental data generated from the test stand. The tests were performed at the BorgWarner Poland company (Jasionka, Poland). The model was simulated under the pulsatile mass-flow rate of the exhaust gases from the six-cylinder engine, as seen in Figure 11.

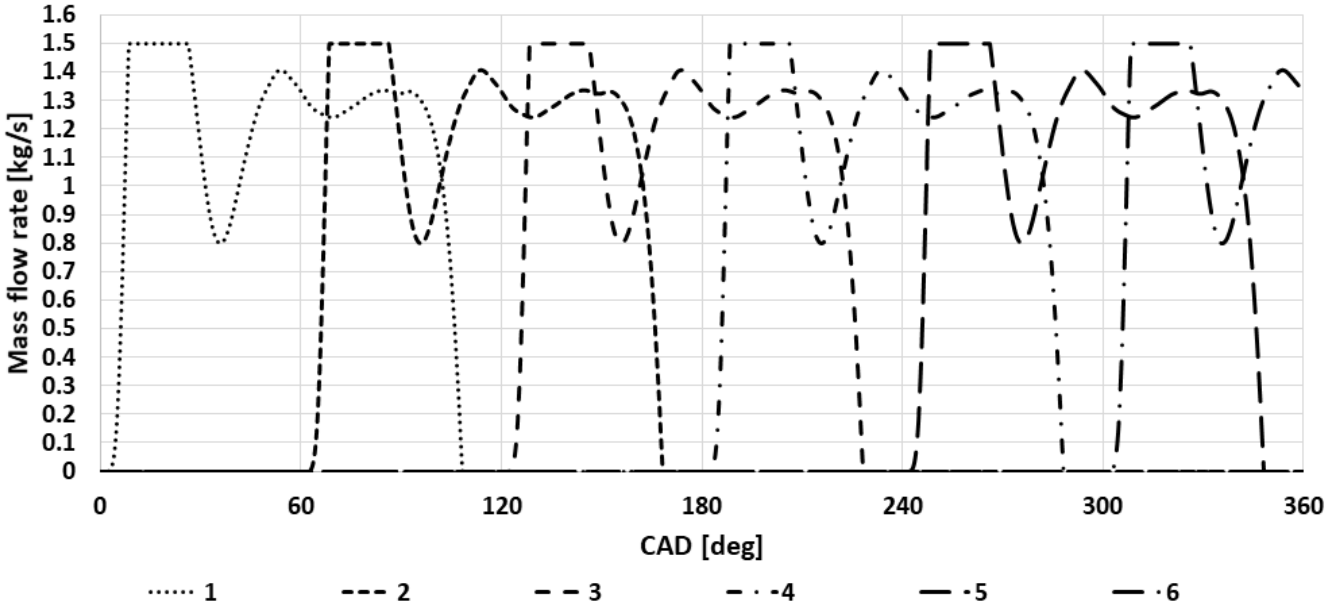

Figure 11. The mass-flow rate boundary conditions at the inlet to the six exhaust pipes during the single revolution of the crankshaft.

From Figure 11, one can see that the mass flow rate of exhaust gases changes from 0 to 1.5 kg/s during the revolution of the crankshaft represented by the crank angle degree (CAD). Such high mass-flow rate values exceeded automotive radial turbines' possibilities. Thus, the authors used rotor A, which had an inlet diameter of 140 mm, and the scaled model of rotor B to investigate the performance of the two-stage turbine system. Rotor A was provided by BorgWarner Polska company and was used as a baseline for the numerical simulation. It was an older version of radial turbines. On the other hand, rotor B was one of the latest generations of radial turbines. Rotor B was scaled to match the dimensions of rotor A to compare both rotors in a two-stage turbine system. At the outlet, the pressure-outlet boundary condition was used. The location of the inlet and outlet boundary conditions are shown in Figure 12. The parameters of the boundary conditions are shown in Table 4.

Table 4. The parameters of the boundary conditions.

Inlet Boundary Condition	
Boundary condition type	Mass-flow rate
Mass-flow rate values (kg/s)	0 ÷ 1.5
Inlet temperature (K)	700
Gauge-pressure (Pa)	300,000
Outlet Boundary Condition	
Boundary condition type	Pressure outlet
Outlet pressure (Pa)	100,000
Outlet temperature (K)	500

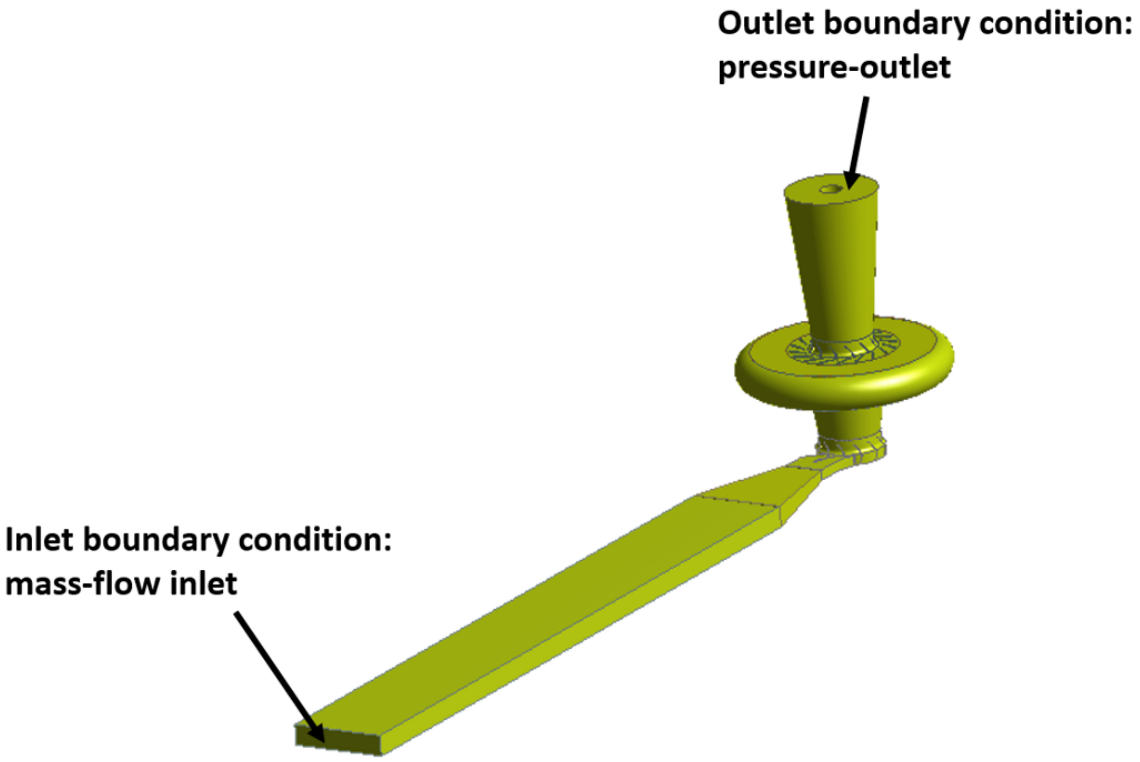

Figure 12. The position of the inlet and outlet boundary conditions [25].

4.4. Mesh Validation

To generate accurate results, the numerical mesh had to be validated. The mesh validation was performed during the single revolution of the crankshaft. For validation purposes, the total pressure parameter was used. The mesh validation was performed for a different number of elements on the critical domains: the exhaust pipes, the first-stage rotor, the VTG vanes, and the second-stage rotor. The mesh validation is shown in Figures 13 and 14.

It can be seen that the increase in the elements led to a negligible difference between pressure variations. The total number of elements of the two-stage turbine model with rotors A and B is shown in Table 5.

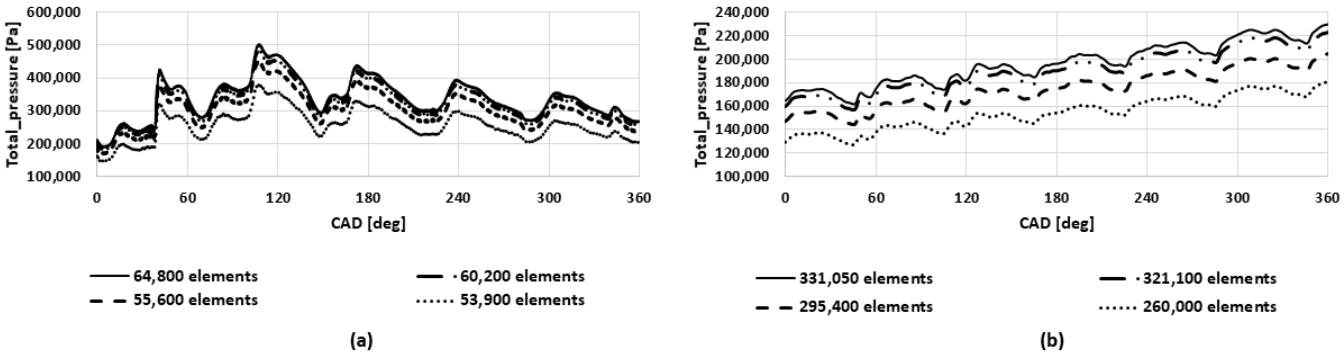

Figure 13. The mesh validation of (**a**) exhaust pipes and (**b**) VTG vanes.

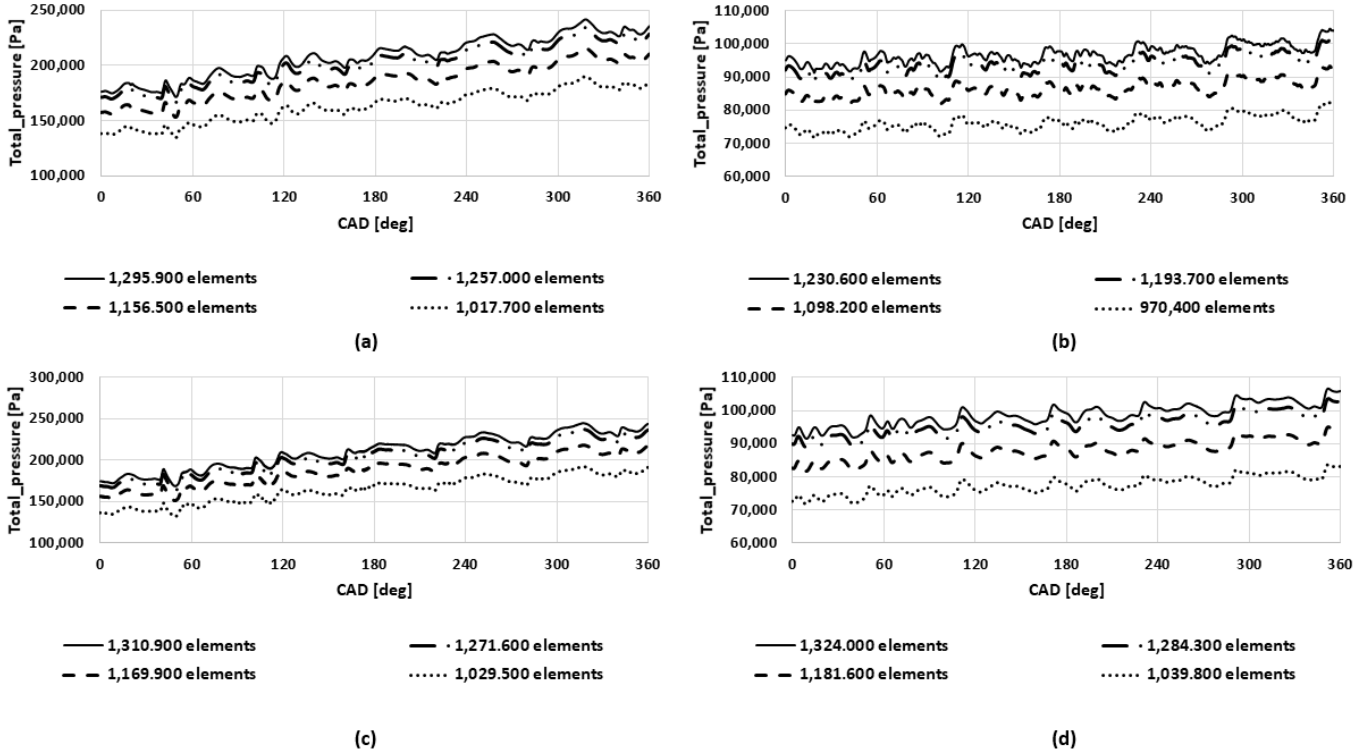

Figure 14. The mesh validation in terms of pressure variation of (**a**) rotor A—first-stage, (**b**) rotor A—second-stage, (**c**) rotor B—first-stage and (**d**) rotor B—second-stage during the single revolution of the crankshaft.

Table 5. The total number of elements of two-stage system with rotor A and rotor B.

Rotor A	
Exhaust pipes domain (×6)	64,800
First-stage rotor domain	1,295,900
Diffuser domain	55,200
Inter-stage pipes domain	536,390
Second-stage rotor domain	1,230,600
Outlet domain	63,000
Total number of elements	3,245,890
Rotor B	
Exhaust pipes domain (×6)	64,800
First-stage rotor domain	1,310,900
Diffuser domain	55,200
Inter-stage pipes domain	536,390
Second-stage rotor domain	1,324,000
Outlet domain	63,000
Total number of elements	3,354,290

4.5. Model Validation

The root mean square error (RMSE) was used for the model validation. The area-averaged total pressure was investigated for three different turbine speeds for validation purposes. The total pressure was measured at the outlet from the second-stage rotor. The RMSE can be calculated as follows:

$$\mathrm{RMSE} = \sqrt{\frac{\sum_{i=1}^{n}\left(X_{obs,i} - X_{model,i}\right)^2}{n}}, \tag{15}$$

The $X_{obs,i}$ is the measured pressure value, while $X_{model,i}$ is the predicted pressure value. The n stands for the number of measurements. The RMSE analysis was performed for rotor A. The experimental test for rotor B was not conducted as the 3-D model of rotor B was scaled up to match rotor A. However, the results were presented during the last crankshaft revolution due to the long measurement period. The RMSE analysis can be seen in Figure 15.

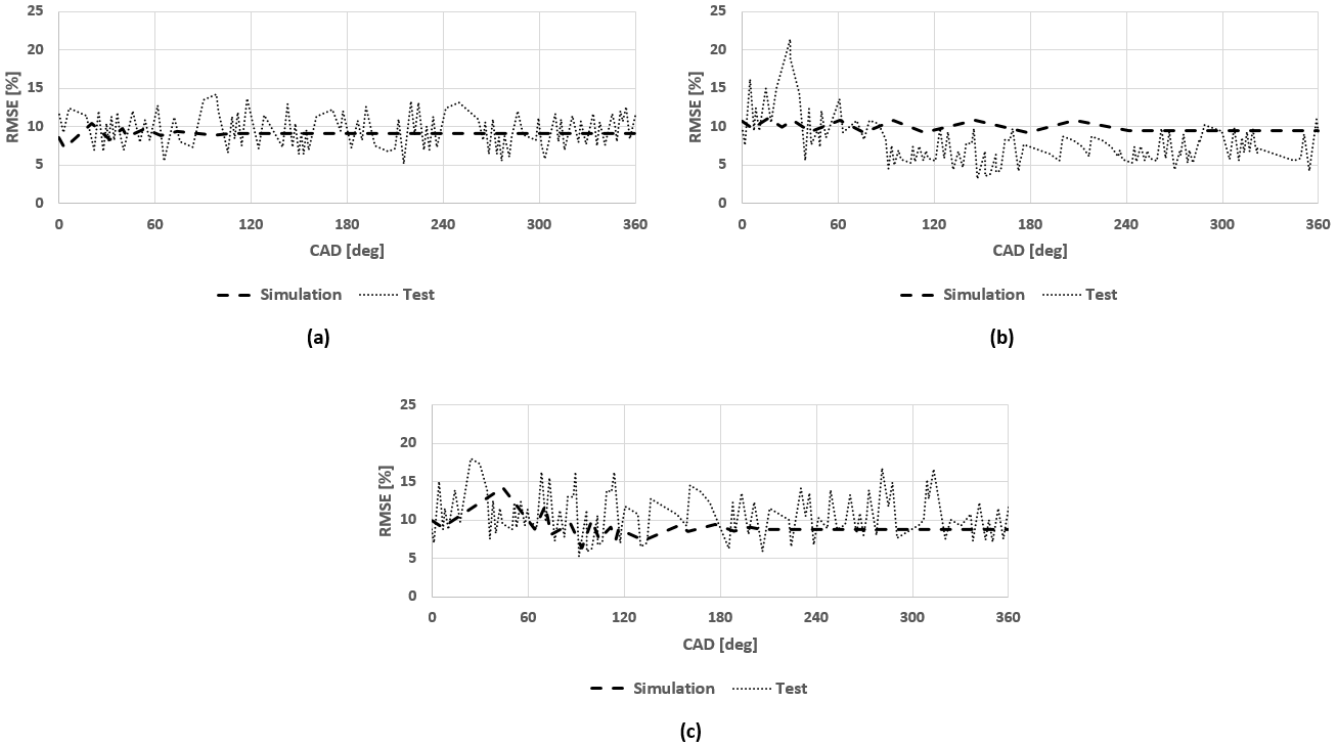

Figure 15. The RMSE analysis of the two-stage turbine system with rotor A turbine at the turbine speed (**a**) 40,000 rpm, (**b**) 50,000 rpm and (**c**) 60,000 rpm.

As can be seen, the variation of RMSE simulation values in area-averaged total pressure was about 9.1%. The simulation error follows the trend of the RMSE test values. Based on such values, the authors concluded that the numerical model could be used for further research.

As previously mentioned, the unsteady simulations are very demanding due to the simulations of the whole rotor domain instead of a single rotor passage. The simulation was performed until the pressure variations at the inlet to the first-stage rotor from each exhaust pipe were identical. Figure 16 illustrates the variation of the total pressure at the inlet from each exhaust pipe.

Figure 16 shows that the pressure variation at the inlet to the first-stage rotor from each exhaust pipe was conducted for nine crankshaft revolutions. The convergence condition was met with identical pressure changes at the inlet to the rotor from each exhaust pipe. Such a condition was achieved during the ninth revolution of the crankshaft. That is why further analysis was presented during the ninth revolution of the crankshaft.

As can be seen, the calculation was very demanding, considering the low value of the time step. Such calculations required a suitable computational machine. The parameters of the computational machine are shown in Table 6.

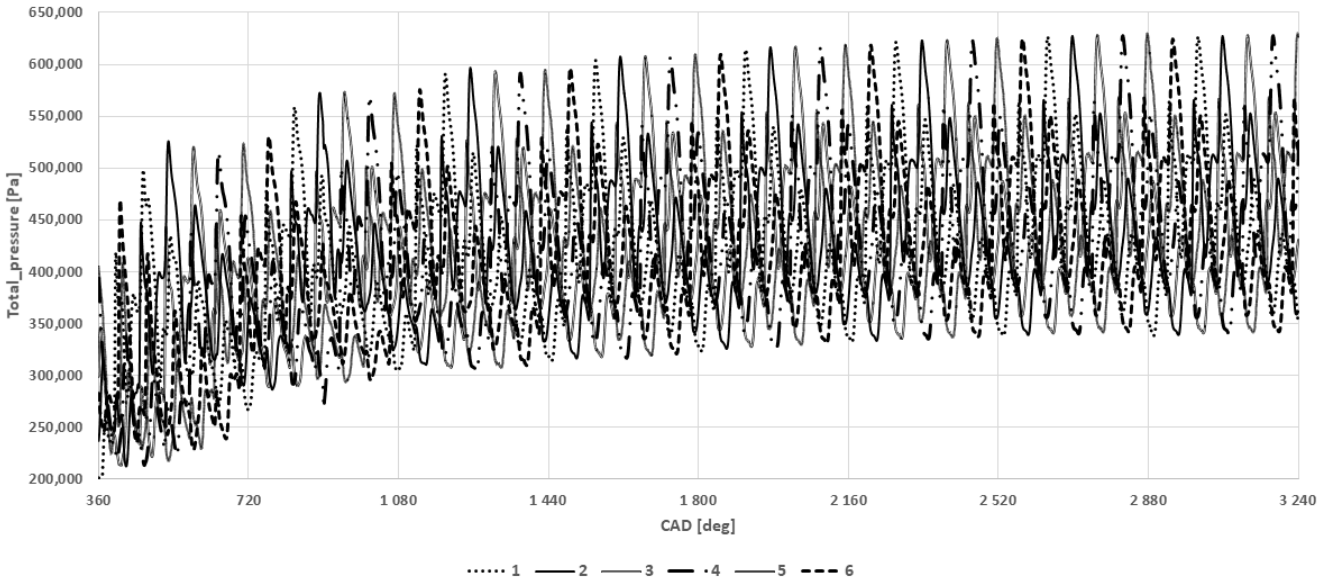

Figure 16. The variation of the pressure at the inlet to the first-stage rotor from each of the six exhaust pipes for nine revolutions of the crankshaft.

Table 6. The parameters of the computational machine.

Computational Machine	
Central Processing Unit (CPU) type	Ryzen 9
Number of CPU cores	9
Random-Access Memory (RAM) (Gb)	128

Despite a relatively fast computing machine, each simulation case was computed within approx. two weeks to meet the convergence conditions.

5. Results and Discussion

As previously mentioned, the results of the numerical simulations were presented during the ninth revolution of the crankshaft.

The first-stage rotor was periodically supplied with the exhaust gases according to the engine firing order. That is why the exhaust pulses from each exhaust pipe could be placed on the single plot represented by the quasi-constant pressure with variations within a specific, constant range. The superposition of pressure plots of each exhaust pipe from Figure 16 can be seen in Figure 17.

It can be observed that the first-stage rotor was constantly supplied with the quasi-constant change of exhaust gases at its circumference. The pressure values changed within the constant range during the ninth revolution of the crankshaft. Such a phenomenon was identical to the modern scroll turbines in which the pressure distribution along the volute circumference should be identical.

5.1. Separation of Exhaust Gases at the Inlet to the First-Stage Rotor

The separation of the exhaust gases at the first-stage rotor was investigated based on the mass-flow rate variation from two adjacent exhaust pipes and the rotor gap between those pipes. To monitor the leakage of the exhaust gases between the adjacent exhaust pipes, a particular interface was created at the center of the rotor gap domain, as shown in Figure 18.

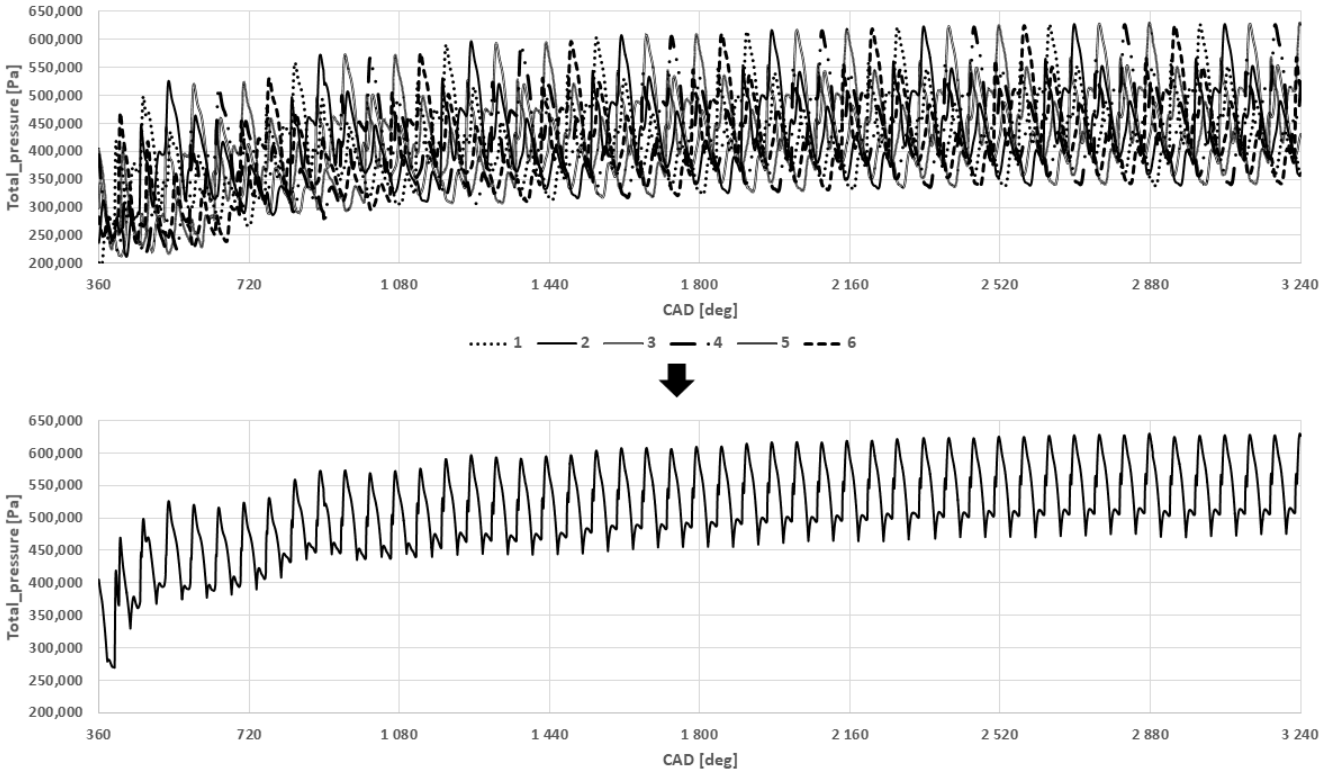

Figure 17. The superposition of the pressure plots at the inlet to the first-stage rotor for nine revolutions of the crankshaft.

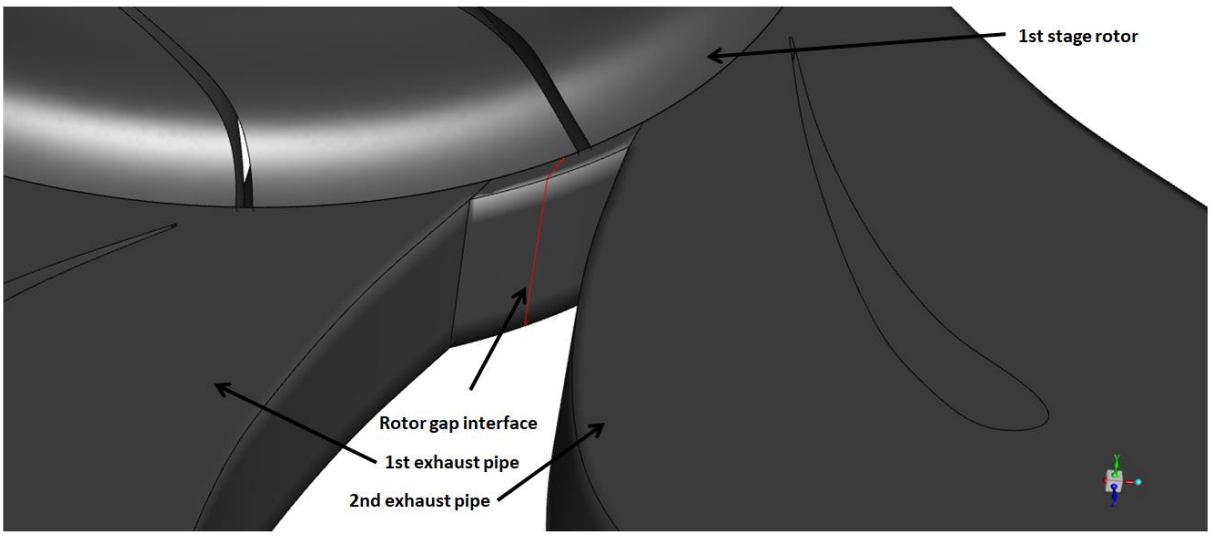

Figure 18. The position of the mass-flow rate monitor at the rotor gap domain.

The detailed leakage analysis of the exhaust gases is shown in Figure 19.

Figure 19 shows a leakage phenomenon between the adjacent exhaust pipes through the rotor gap.

The dashed plot lines present the variation from the adjacent exhaust pipes 1 and 2. Each pipe exhaust valve's opening and closure period were marked with circular and rectangular points. The pipe 1 exhaust valve opened at 40 CAD, while the closure occurred at 143 CAD. The pipe 2 exhaust pipe opened at 110 CAD, and the closure occurred at 210 CAD. The bottom plot line shows the variation of the exhaust mass flow rate at the interface of the rotor gap. It can be seen that between the opening (A1) and closure (A2) of the pipe 1 exhaust valve, the mass flow of the exhaust gases through the rotor gap increased

from 0.05 kg/s to 0.1 kg/s. Such a phenomenon occurred until the closure of the pipe 1 exhaust valve. It can be seen that the opening of the pipe 2 exhaust valve had minor effects on the mass flow rate through the gap. It was caused by the low value of the first pulse of the exhaust gases right after the opening of the exhaust valve. After the closure of the pipe 1 exhaust valve, the pipe 2 mass flow rate had the dominant effect on the flow rate through the rotor gap. As the pipe 1 exhaust valve opened, the pipe 2 exhaust mass-flow rate dropped from 0.24 to 0.15 kg/s. Such a drop was the effect of the leakage between the exhaust pipes. However, as the pipe 2 exhaust valve opened, the flow rate increased from 0.14 to 0.43 kg/s. The pipe 2 flow rate decreased for a shorter period of time compared to the leakage through the rotor gap.

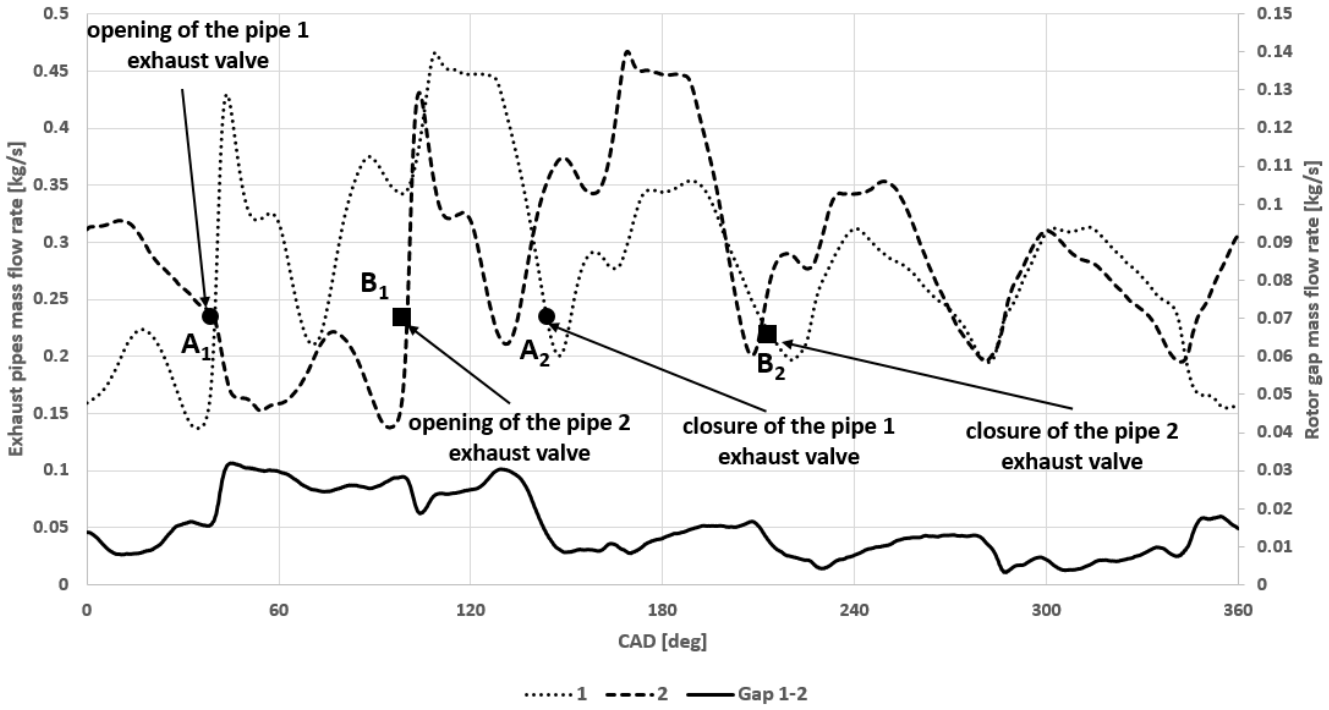

Figure 19. The variation of exhaust mass-flow rate at the inlet to the first-stage rotor from two adjacent exhaust pipes no 1 and 2 and at the rotor gap between those pipes.

The results of the exhaust mass-flow rate analysis through the rotor gap are shown in Figure 20.

The gas mass-flow rate changes follow the same pattern for each case. The exhaust mass-flow rate significantly dropped at 110 CAD. Such a flow-rate drop was related to the pipe 2 exhaust valve opening, which disturbed the flow through the rotor gap. The two rotor geometries showed almost no significant gas flow rate changes at the same turbine speed. The plots presented in Figure 20a,b were almost the same.

On the other hand, significant differences were observed at different turbine speeds with the same rotor geometry. Figure 20a,c show that the peak value of the exhaust mass-flow rate decreased from 0.039 kg/s to 0.032 kg/s. The lowest peak value of exhaust mass-flow rate for rotor A was observed at the 40,000 rpm case. The same pattern was observed for rotor B. The lowest leakage conditions for rotors A and B were observed at the 40,000 rpm case. The authors speculate that such observations might be related to the lower value of the blade tip velocity, which reduced the tangential velocity of the exhaust gases at the inlet to the first-stage rotor. In addition, the position of the VTG vanes impacted the exhaust gases' mass-flow rate. It can be observed that the closure of the VTG vanes caused a minor increase in the gas flow rate, resulting in increased leakage. Such a phenomenon was caused by the upstream position of the rotor gaps from the VTG vanes domain. The closure of the VTG vanes caused an increase in the pressure upstream from

the VTG domain. Thus, the increased backpressure prevented the escape of the exhaust gases through the first-stage rotor, leading to the increased flow rate through the rotor gap. The total leakage values through the six rotor gaps during the single revolution of the crankshaft are shown in Table 7.

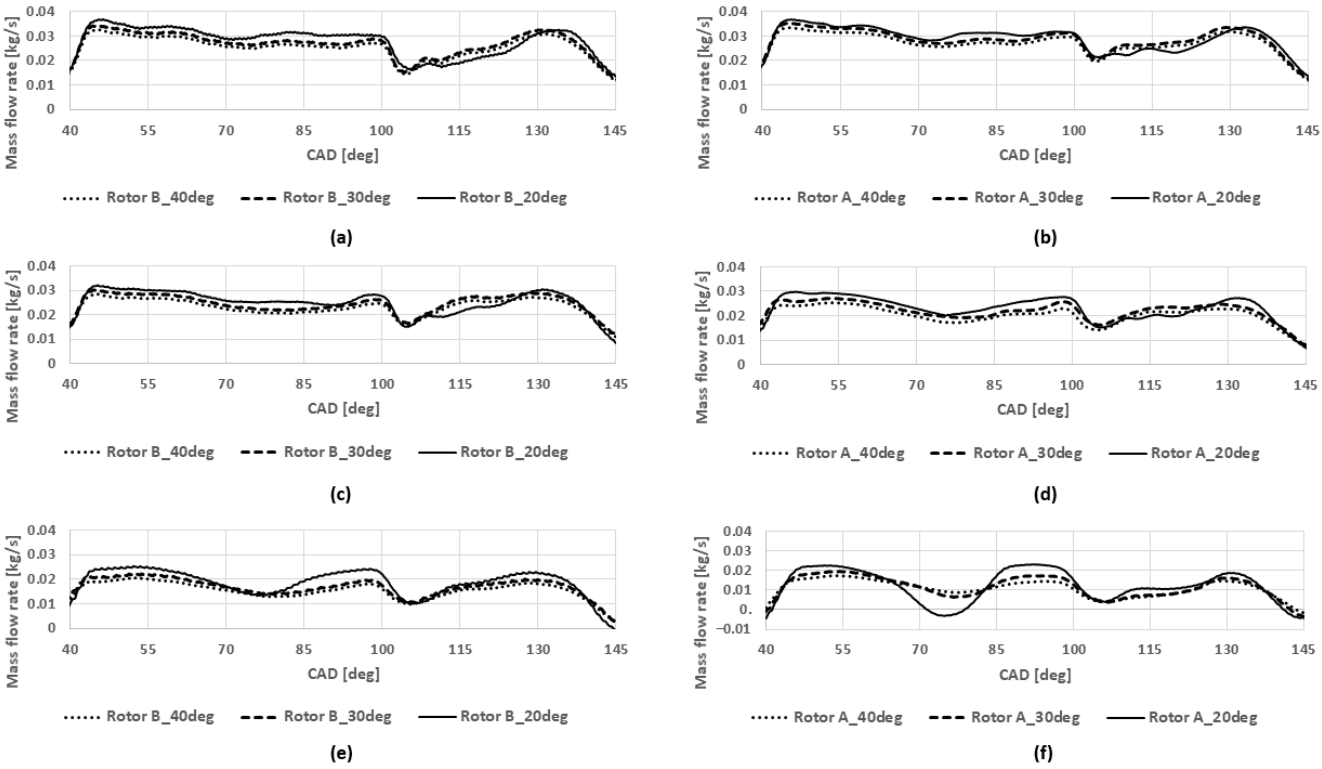

Figure 20. The changes of exhaust mass flow rate at the rotor gap interface for three different turbine speeds, VTG vane positions and rotor geometries (**a**) rotor B at 60,000 rpm, (**b**) rotor A at 60,000 rpm, (**c**) rotor B at 50,000 rpm, (**d**) rotor A at 50,000 rpm, (**e**) rotor B at 40,000 rpm, (**f**) rotor A at 40,000 rpm.

Table 7. The total leakage values of the exhaust gases' mass-flow rate though the rotor gaps during the single revolution of the crankshaft.

Rotor A			Rotor B		
Turbine Speed (rpm)	**VTG Vanes Angle (deg)**	**Exhaust Mass-Flow Rate (kg/s)**	**Turbine Speed (rpm)**	**VTG Vanes Angle (deg)**	**Exhaust Mass-Flow Rate (kg/s)**
60,000	40	0.094	60,000	40	0.087
	30	0.099		30	0.091
	20	0.101		20	0.094
50,000	40	0.068	50,000	40	0.070
	30	0.075		30	0.074
	20	0.078		20	0.075
40,000	40	0.031	40,000	40	0.029
	30	0.032		30	0.031
	20	0.037		20	0.033

The lowest value of the exhaust mass-flow rate was observed for the 40,000 rpm case. For this case, 7.4% to 10.1% of the exhaust pipes' total mass-flow rate was wasted through the rotor gap during the single revolution of the crankshaft. It can be seen that slightly lower leakage values were observed for the two-stage system with rotor B geometry.

5.2. The Inlet to the First-Stage Rotor

As mentioned above, the first-stage rotor is supplied with quasi-constant pressure at the inlet through the whole circumference of the rotor. It was caused by the short periods between the exhaust pulses for the six-cylinder engine. For research purposes, the pressure and temperature changes at the rotor inlet were investigated as the critical parameters of the turbine performance. The area-averaged pressure and temperature values were measured at the monitor surface between the first-stage nozzle vane domain and the first-stage rotor domain. The results were presented during the last crankshaft revolution as the converge conditions were met on the ninth revolution of the crankshaft. The area-averaged pressure variations are shown in Figure 21.

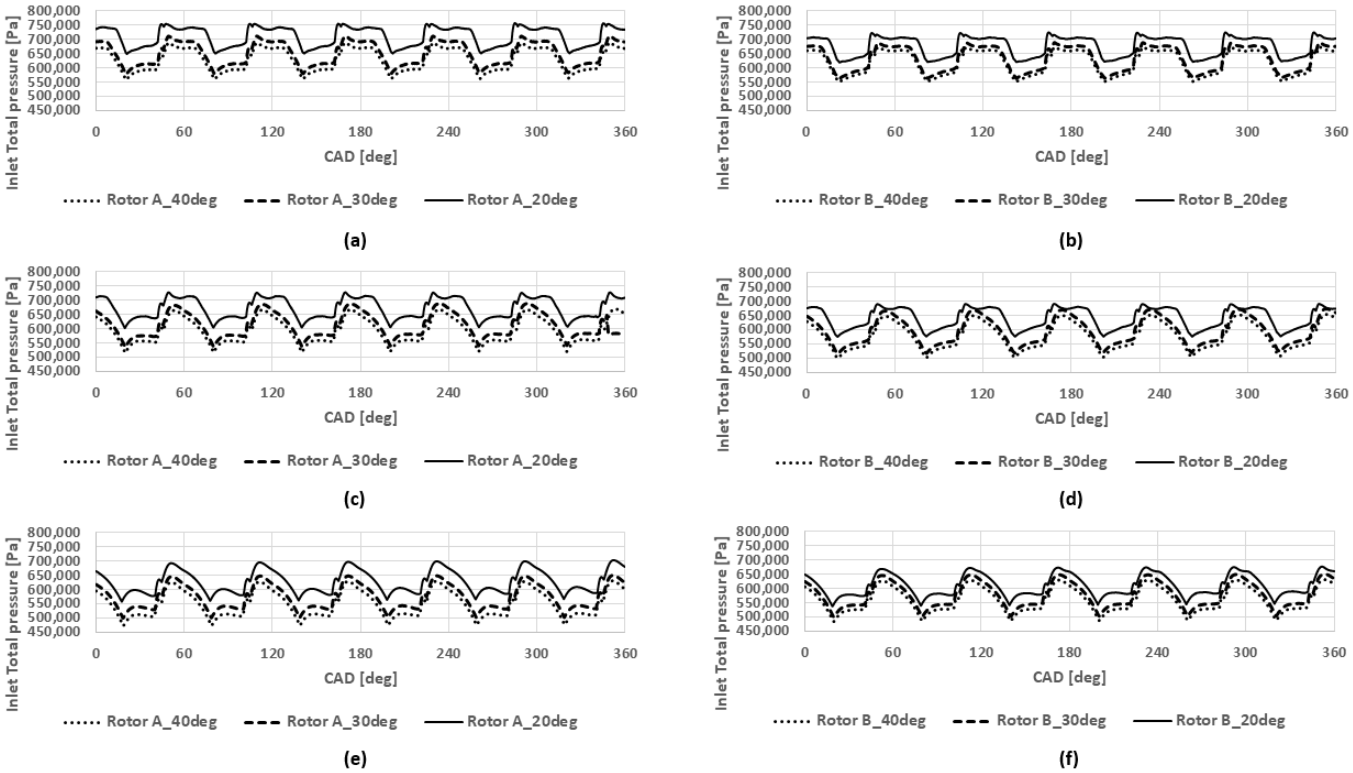

Figure 21. The area-averaged pressure changes at the inlet to the first-stage rotor during the single revolution of the crankshaft for three different turbine speeds, VTG vane positions and rotor geometries: (**a**) rotor A at 60,000 rpm, (**b**) rotor B at 60,000 rpm, (**c**) rotor A at 50,000 rpm, (**d**) rotor B at 50,000 rpm, (**e**) rotor A at 40,000 rpm, (**f**) rotor B at 40,000 rpm.

Figure 21 shows the pressure variations at the inlet to the first-stage rotor during the single revolution of the crankshaft for two geometries of the turbine rotors and different VTG vane positions. It can be seen that the pressure changes were quasi-constant within the constant range through the whole revolution of the crankshaft. For every turbine speed, rotor B provided lower pressure values at the inlet, as it had 11 blades compared to the 12 of rotor A. This phenomenon caused lower flow restriction through the turbine system downstream from the first-stage rotor. The average pressure differences between the rotor A and B cases were about 10% for each turbine speed. Additionally, one can see that the inlet pressure decreased with the decrease in the turbine speed. Such a situation occurred for both rotor A and rotor B geometries. However, the closure of the VTG vanes had the opposite effect on the pressure changes. It can be seen that the inlet pressure increased with the closure of the VTG vanes. Such a phenomenon was similar to the mass-flow rate changes through the rotor gap as the closure of the VTG vanes caused flow restrictions in the upstream direction from the VTG vanes domain. The highest pressure values were observed for the 20° angle of the VTG vanes at each turbine speed. Figure 21b,d,f shows

that the differences in rotor B pressure changes for each VTG position were lower than the rotor A plots. The authors concluded that the rotor B geometry at the first stage was less affected by the closure of the VTG vanes than rotor A.

The area-averaged changes in the total temperature at the inlet to the first-stage rotor can be seen in Figure 22.

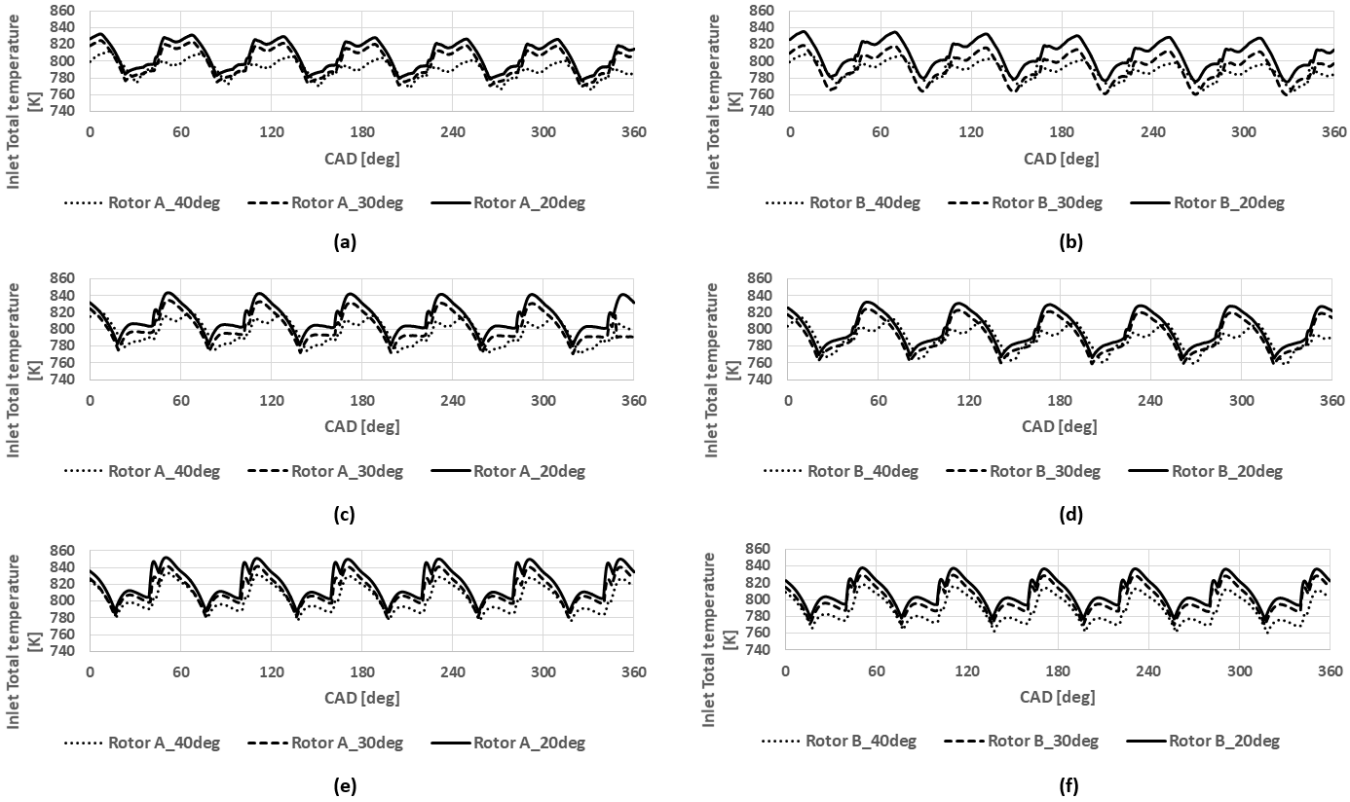

Figure 22. The variations of the area-averaged total temperature at the inlet to the first-stage rotor during the single revolution of the crankshaft for three different turbine speeds, VTG vane positions and rotor geometries: (**a**) rotor A at 60,000 rpm, (**b**) rotor B at 60,000 rpm, (**c**) rotor A at 50,000 rpm, (**d**) rotor B at 50,000 rpm, (**e**) rotor A at 40,000 rpm, (**f**) rotor B at 40,000 rpm.

As can be seen, the area-averaged total temperature changed in a quasi-constant manner during the last revolution of the crankshaft. Significant temperature changes were observed at different positions of the VTG vanes for every turbine speed and rotor geometry. The closure of VTG led to increased inlet temperature values which promoted the decrease in turbine performance. The turbine speed was another factor that affected the inlet temperature changes. It can be seen that the decrease in the turbine speed increased the inlet temperature values. Such an increase in the inlet temperature contributed to the turbine performance deterioration. The highest temperature values were observed at the 20° VTG position and 40,000 rpm case for both rotor geometries. For the rotor A and B geometries, the highest temperature values were 851.9 K and 837.9 K, respectively. It is evident that rotor B efficiently utilized energy from the exhaust gases as the inlet temperature values were lower than the rotor A geometry.

5.3. The Outlet from the First-Stage Rotor

The authors followed the previous analysis and investigated the flow parameters at the outlet from the first-stage rotor. The pressure and temperature changes were investigated during the single revolution of the crankshaft. The changes in the area-averaged total pressure at the outlet from the first-stage rotor are shown in Figure 23.

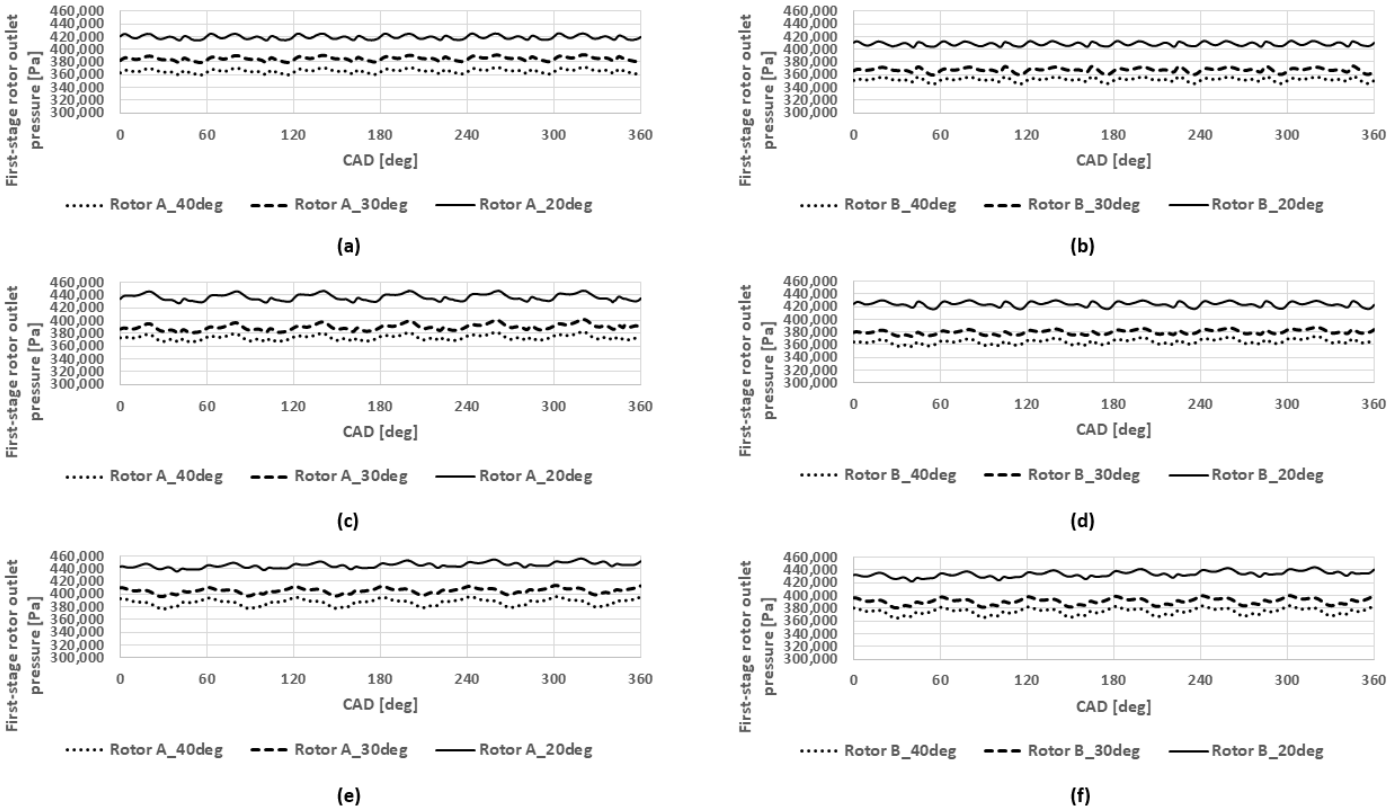

Figure 23. The plots of the area-averaged total pressure at the outlet from the first-stage rotor during the single revolution of the crankshaft for three different turbine speeds, VTG vane positions and rotor geometries: (**a**) rotor A at 60,000 rpm, (**b**) rotor B at 60,000 rpm, (**c**) rotor A at 50,000 rpm, (**d**) rotor B at 50,000 rpm, (**e**) rotor A at 40,000 rpm, (**f**) rotor B at 40,000 rpm.

Figure 23 shows the variations of the area-averaged total pressure at the outlet from the first-stage rotor for two rotor geometries at three turbine speeds and three positions of VTG vanes. It can be observed that the outlet pressure was quasi-constant during the single revolution of the crankshaft. The decrease in pressure fluctuations was evident when compared to the pressure changes shown in Figure 21, which suggested that the flow was less chaotic at the outlet from the first-stage rotor. As the turbine speed decreased for both rotor geometries, an increase in outlet pressure values was observed. Such a phenomenon was evident as both rotors operated more efficiently at higher turbine speeds. Thus, lowering the turbine speeds led to a decrease in the turbine performance. A strong influence of the VTG position on the outlet pressure was observed. The closure of the VTG vanes promoted the increase in outlet pressure. The highest increase was observed for the 20° position of the VTG vanes in each case. The average pressure increase from the 40° VTG position to the 30° VTG position was 1.3%.

On the other hand, the average pressure increase was 13% for 20° VTG from the 30° VTG position. By comparing the plots from Figure 23a to Figure 23b, Figure 23c to Figure 23d, and Figure 23e to Figure 23f, one can see that rotor B generated lower values at the outlet. The average outlet pressure differences between rotors A and B were 5% for each case. The rotor B geometry provided better expansion of the exhaust gases, thus providing higher energy recovery of the exhaust gases. The averaged PR values of the first-stage rotor during the single revolution of the crankshaft are shown in Table 8.

Table 8. The averaged values of the first-stage rotor PR during single revolution of the crankshaft for two rotor geometries, three VTG positions and three turbine speeds.

Rotor A			Rotor B		
Turbine Speed (rpm)	**VTG Vanes Angle (deg)**	**Average Pressure Ratio (-)**	**Turbine Speed (rpm)**	**VTG Vanes Angle (deg)**	**Average Pressure Ratio (-)**
60,000	40	1.72	60,000	40	1.80
	30	1.68		30	1.77
	20	1.66		20	1.71
50,000	40	1.59	50,000	40	1.63
	30	1.57		30	1.62
	20	1.54		20	1.56
40,000	40	1.42	40,000	40	1.53
	30	1.41		30	1.52
	20	1.38		20	1.45

The first-stage rotor B geometry provided a higher pressure ratio for each turbine speed and VTG position when compared to the rotor A geometry. The PR of both rotors decreased with the turbine speed. The same phenomenon was observed with the closure of the VTG vanes.

Figure 24 shows the area-averaged values of the total temperature at the outlet from the first-stage rotor for two different rotor geometries, three turbine speeds, and VTG positions.

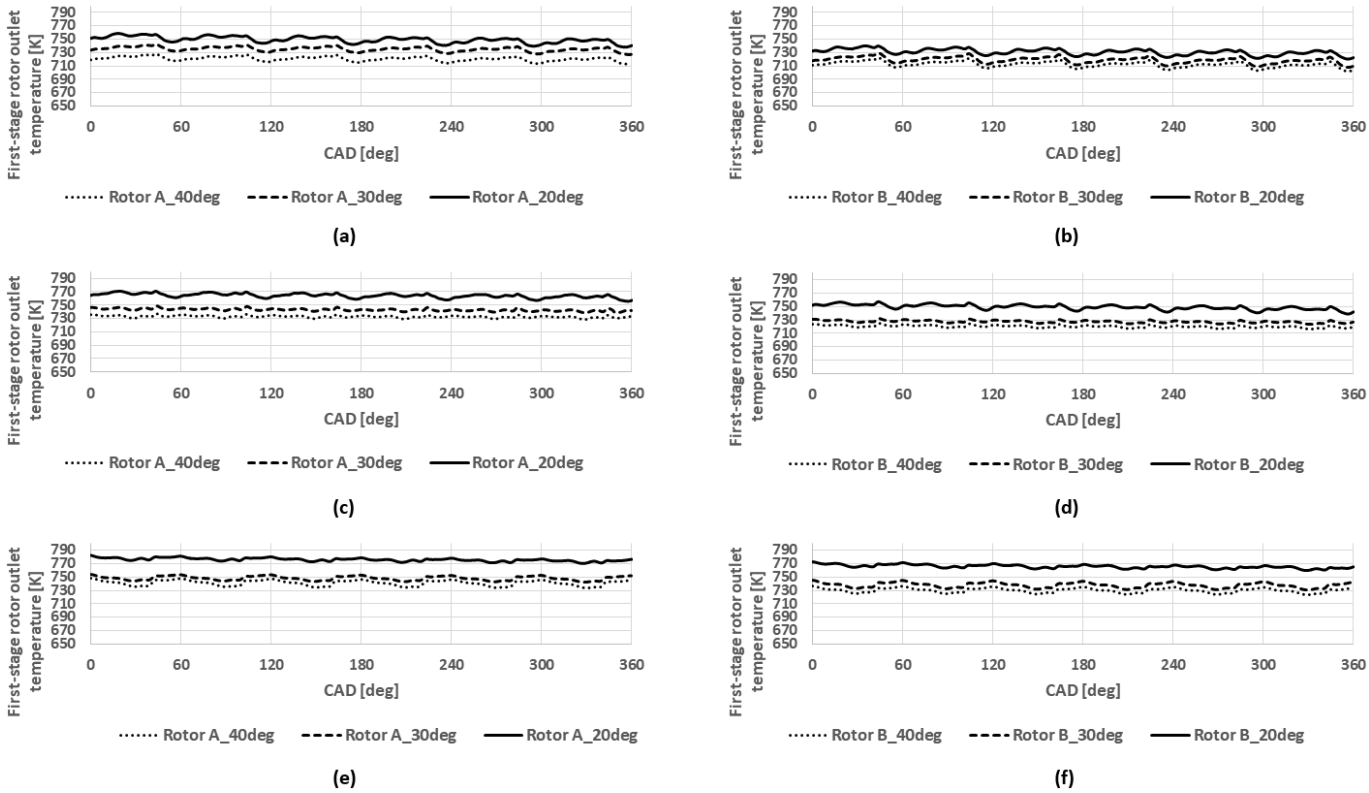

Figure 24. The variation of area-averaged total temperature at the outlet from the first-stage rotor during the single revolution of the crankshaft for three different turbine speeds, VTG vane positions and rotor geometries: (**a**) rotor A at 60,000 rpm, (**b**) rotor B at 60,000 rpm, (**c**) rotor A at 50,000 rpm, (**d**) rotor B at 50,000 rpm, (**e**) rotor A at 40,000 rpm, (**f**) rotor B at 40,000 rpm.

The area-averaged temperature values oscillated within a constant range, which indicated that the convergence conditions were met at the last revolution of the crankshaft. Reduced temperature fluctuations were observed at the outlet from the first-stage rotor compared to the inlet temperature changes. The lowered temperature values at the outlet indicated that both rotors recovered energy from the exhaust gases. However, a slightly better heat recovery was observed for the rotor B geometry as the outlet temperature was lower than the rotor A geometry for every turbine speed. The temperature variations followed the same pattern as the rotor outlet pressure changes shown in Figure 23; with the decrease in the turbine speed, the rotor outlet temperature increased, decreasing the turbine performance. In addition, the closure of the VTG vanes caused an increase in the outlet temperature. The temperature increased by 2% and 5% for the 30° and 20° VTG cases, respectively. The average temperature drop at the first-stage rotor is shown in Table 9.

Table 9. The average temperature drop at the first-stage rotor for two different rotor geometries, three turbine speeds and VTG positions.

Rotor A			Rotor B		
Turbine Speed (rpm)	**VTG Vanes Angle (deg)**	**Average Temperature Drop (K)**	**Turbine Speed (rpm)**	**VTG Vanes Angle (deg)**	**Average Temperature Drop (K)**
60,000	40	69.80	60,000	40	77.77
	30	63.56		30	72.59
	20	57.28		20	76.67
50,000	40	64.15	50,000	40	69.71
	30	58.73		30	64.56
	20	49.35		20	51.04
40,000	40	62.45	40,000	40	65.26
	30	64.59		30	69.96
	20	44.71		20	49.70

The table shows that the temperature drop was higher for the rotor B case. However, only minor temperature differences were observed for rotors A and B. On the other hand, the closure of the VTG vanes clearly showed the first-stage rotor performance limitation.

5.4. The Outlet from the Second-Stage Rotor

A detailed analysis was carried out for the second-stage rotor as the rotor domain was positioned downstream from the VTG domain. To accurately investigate the rotor performance, the time phase shift was included in the research. The outlet parameters from the first-stage rotor were used as the inlet parameters at the second-stage rotor. The authors justified such an approach with the low pressure losses through the inter-stage pipes. The pressure losses were between 1.2 and 3.2%. The area-averaged total pressure and total temperature were used for the second-stage rotor analysis.

Figure 25 shows the area-averaged outlet pressure from the second-stage rotor during the single revolution of the crankshaft. Quasi-constant outlet pressure changes were observed during the crankshaft's single revolution. In terms of turbine speed, the pressure change pattern was similar to the changes in Figure 23. With the decrease in turbine speed, the outlet pressure increased, which was related to the lower expansion possibilities of the rotor at lower speeds. On the other hand, the opposite pattern was observed for the positioning of the VTG vanes. With the closure of the VTG vanes, the outlet pressure decreased. The lowest pressure values for each case were observed for the 20° VTG position.

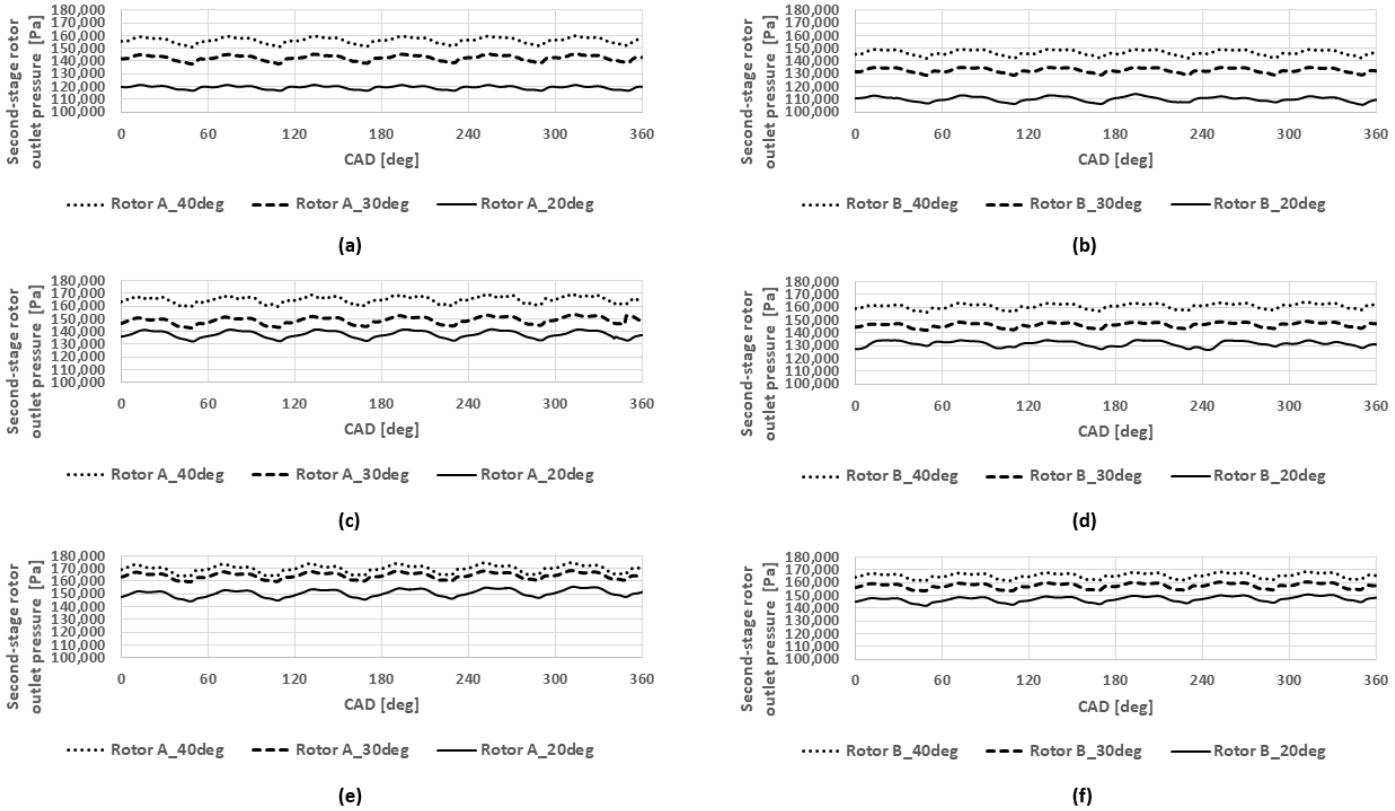

Figure 25. The plots of area-averaged total pressure at the outlet from the second-stage rotor during the single revolution of the crankshaft for three different turbine speeds, VTG vane positions and rotor geometries: (**a**) rotor A at 60,000 rpm, (**b**) rotor B at 60,000 rpm, (**c**) rotor A at 50,000 rpm, (**d**) rotor B at 50,000 rpm, (**e**) rotor A at 40,000 rpm, (**f**) rotor B at 40,000 rpm.

In contrast to the first-stage rotor domain, the second-stage rotor domain was placed downstream from the VTG domain. Thus, the change of the VTG vanes' position resulted in the opposite effect on the second-stage rotor performance. Overall, the lowest values of the outlet pressure of the second-stage rotor were observed for the 60,000 rpm case and 20° VTG position. The rotor B geometry provided lower values of the outlet pressure at each turbine speed. Such a phenomenon was caused by the lower pressure losses inside the rotor B passages. The second-stage rotor PR values are shown in Table 10.

Table 10. The average PR of the second-stage rotor for two rotor geometries, three different turbine speeds and VTG positions.

Rotor A			Rotor B		
Turbine Speed (rpm)	**VTG Vanes Angle (deg)**	**Average Pressure Ratio (-)**	**Turbine Speed (rpm)**	**VTG Vanes Angle (deg)**	**Average Pressure Ratio (-)**
60,000	40	2.23	60,000	40	3.07
	30	2.58		30	3.13
	20	3.41		20	3.62
50,000	40	2.16	50,000	40	3.17
	30	2.49		30	3.08
	20	3.02		20	3.22
40,000	40	2.17	40,000	40	2.94
	30	2.36		30	2.91
	20	2.87		20	3.14

The PR of the second-stage rotor increased with the closure of the VTG vanes. Notable differences were also observed between the PR values of the first- and second-stage rotors. The PR of the second-stage rotor was almost two times higher than that of the first-stage rotor shown in Table 8. Rotor B generated higher PR values for every case, showing that next-generation geometry performs better than the older geometry version.

The area-averaged total temperature at the outlet from the second-stage rotor is shown in Figure 26.

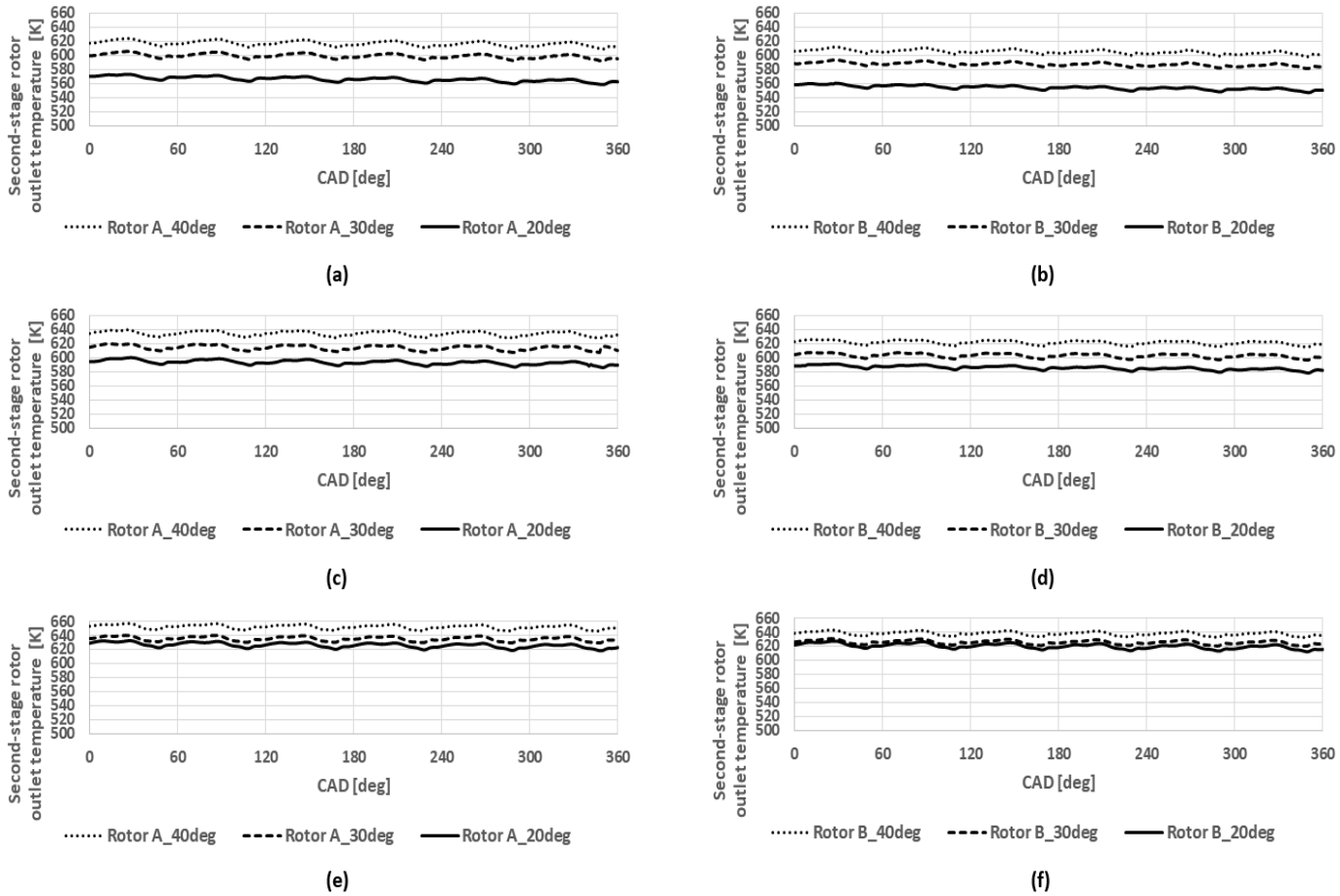

Figure 26. The area-averaged plots of total temperature at the outlet from the second-stage rotor: (**a**) rotor A at 60,000 rpm, (**b**) rotor B at 60,000 rpm, (**c**) rotor A at 50,000 rpm, (**d**) rotor B at 50,000 rpm, (**e**) rotor A at 40,000 rpm, (**f**) rotor B at 40,000 rpm.

The temperature fluctuations at the outlet from the second-stage rotor were lower than the temperature changes at the outlet from the first-stage rotor shown in Figure 24. For both rotor A and rotor B geometries, the lowest temperature value was observed for the 60,000 rpm case and 20° VTG position, as the rotor efficiency increased with the turbine speed. The VTG closure also enhanced both geometries' expansion possibilities, which was already pointed out in Figure 25. However, slightly lower temperature values were observed for rotor B, which meant that rotor B recovered a higher amount of heat energy from the exhaust gases. The average values of the outlet temperature from the second-stage rotor are shown in Table 11.

Table 11. The average values of the outlet temperature from the second-stage rotor for two different rotor geometries.

Rotor A			Rotor B		
Turbine Speed (rpm)	**VTG Vanes Angle (deg)**	**Average Temperature Drop (K)**	**Turbine Speed (rpm)**	**VTG Vanes Angle (deg)**	**Average Temperature Drop (K)**
60,000	40	84.85	60,000	40	131.37
	30	118.21		30	155.69
	20	166.36		20	167.60
50,000	40	79.63	50,000	40	123.28
	30	110.32		30	148.15
	20	152.88		20	169.60
40,000	40	69.33	40,000	40	110.04
	30	92.84		30	129.56
	20	130.84		20	157.74

Table 11 shows that the temperature drop of the second-stage rotor was higher than the temperature drop from the first-stage rotor. Thus, the second-stage rotor provided higher heat recovery from the exhaust gases than the first-stage rotor. A higher temperature drop was also observed for the rotor B geometry as fewer flow losses were observed in the rotor passages.

The authors concluded that the first-stage rotor provided lower expansion capabilities than the second-stage rotor due to the negative influence of the VTG vanes. As the VTG vanes were positioned in a closed position, a significant pressure increase was observed in the upstream direction from the VTG vanes domain. Thus, the pressure at the outlet from the first-stage rotor increased, which limited its expansion capabilities. The reduction of the PR was observed for the first-stage rotor at the lower values of VTG positions. On the other hand, the second-stage rotor performance improved with the closure of the VTG vanes as the second-stage rotor domain was placed in the downstream direction from the VTG domain. The closure of the VTG vanes enhanced its expansion capabilities by increasing its PR and temperature drop. Both rotor geometries provided a significant pressure drop at the first and second stages. However, rotor B provided slightly better expansion possibilities due to lower flow losses through the rotor passage.

5.5. The Tangential Velocity Analysis

The tangential velocity analysis was performed to inspect the flow structure at the outlet from the first- and second-stage rotor. Based on the authors' experience, the flow at the outlet from the rotor should be undisturbed, which means that the tangential component of the absolute velocity should be as low as possible. The turbine velocity triangle is shown in Figure 27.

Figure 27 shows the turbine velocity triangle at the inlet and outlet from the radial turbine. The $\vec{c}_1$ and $\vec{c}_2$ are the vectors of inlet and outlet absolute velocities, $\vec{w}_1$ and $\vec{w}_2$ are the vectors of inlet and outlet relative velocities, $\vec{u}_1$ is the rotor tip linear velocity at the inlet, and $\vec{u}_2$ is the linear tip velocity at the outlet. The $\vec{u}_{c_1}$ and $\vec{u}_{w_1}$ are the tangential components of the inlet absolute and relative velocities, respectively. The same tangential components at the outlet are marked with the "2" index: $\vec{u}_{c_2}$ and $\vec{u}_{w_2}$. In this part, the averaged values of $\vec{u}_{c_1}$ and $\vec{u}_{c_2}$ were investigated as those components contribute in the flow configuration. The same vectors with indexes "3" and "4" indicated the velocity at the inlet and outlet of the second-stage rotor. The area-averaged changes of tangential velocity at the outlet from the first-stage rotor for two rotor geometries are shown in Figure 28.

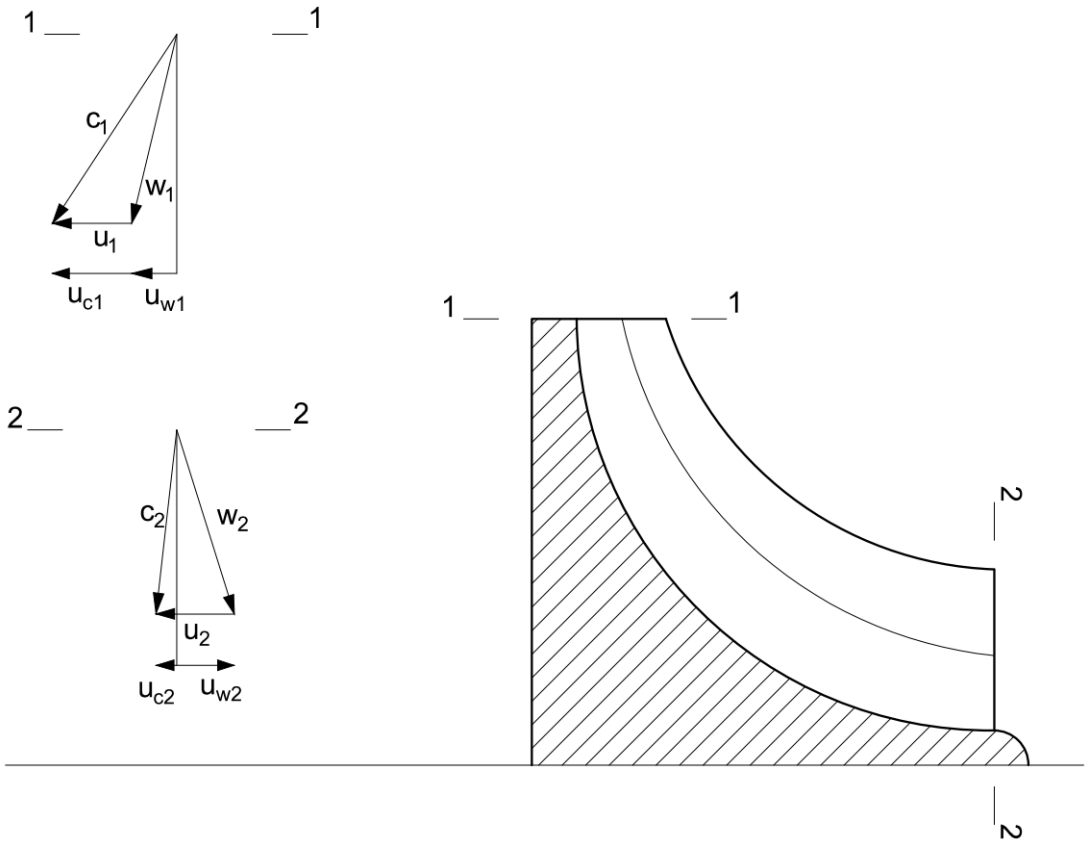

Figure 27. The turbine velocity triangle at the rotor inlet (1—1) and rotor outlet (2—2).

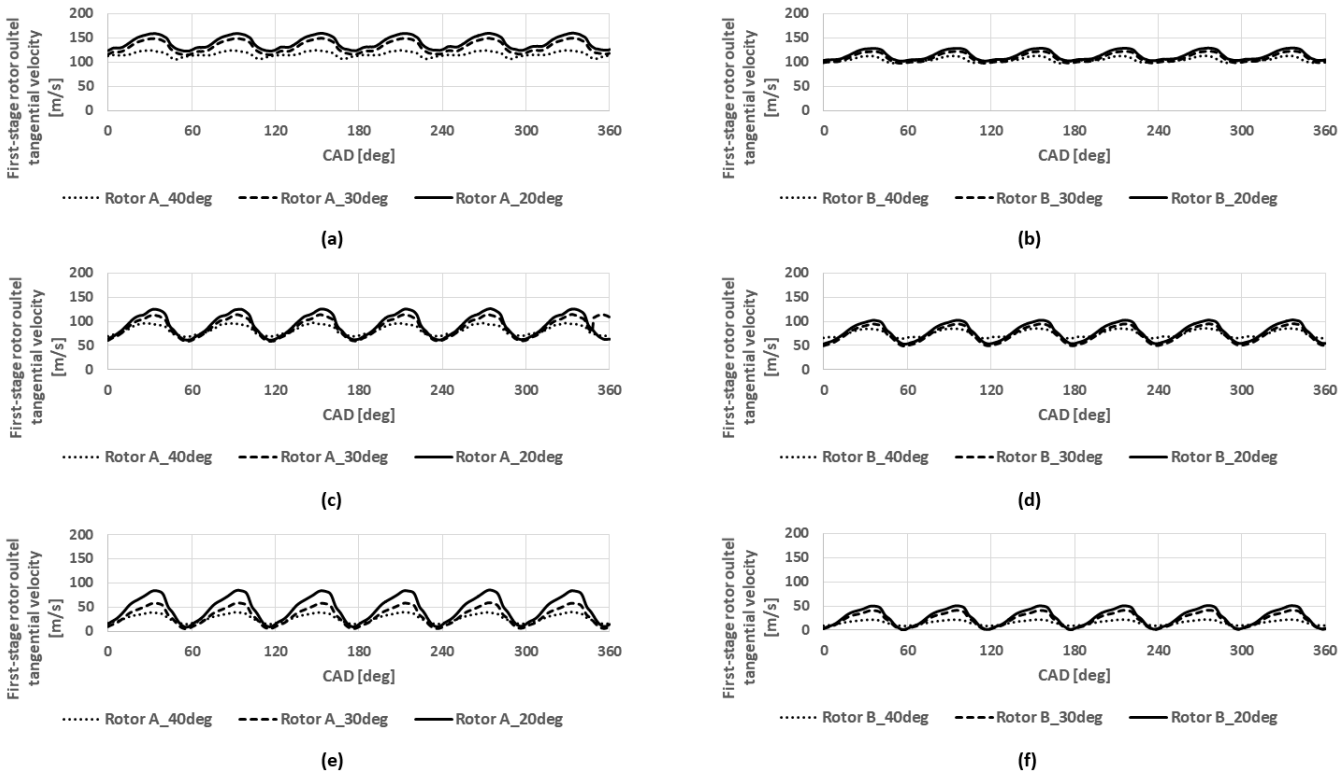

Figure 28. The area-averaged tangential velocity at the outlet from the first-stage rotor: (**a**) rotor A at 60,000 rpm, (**b**) rotor B at 60,000 rpm, (**c**) rotor A at 50,000 rpm, (**d**) rotor B at 50,000 rpm, (**e**) rotor A at 40,000 rpm, (**f**) rotor B at 40,000 rpm.

The outlet tangential velocity dramatically depends on the rotor rotational speed and blade geometry. It can be seen that the absolute tangential velocity decreased with the decrease in the turbine speed for each case. With the outlet's absolute tangential velocity decreasing, the flow became less chaotic at the rotor outlet. However, as previously concluded, the first-stage rotor was more efficient at the high turbine speed. The highest value of the absolute tangential velocity was observed at 60,000 rpm. However, the change of VTG position saw the values of the tangential velocity deteriorate. The closure of the VTG vanes led to increased tangential velocity. Such a pattern agreed with the outlet pressure and temperature changes of the first-stage rotor shown in Figures 23 and 24. The higher the VTG position, the more intensive flow was observed at the outlet from the first-stage rotor. The rotor B geometry case generated lower values of the tangential velocity at the rotor outlet for each turbine speed. The blade geometry of rotor B generated less vortex-like flow at the rotor outlet. The average values of the absolute tangential velocity at the outlet from the first-stage rotor are shown in Table 12.

Table 12. The average values of the tangential velocity at the outlet from the first-stage rotor at different turbine speed and VTG vane positions.

Rotor A			Rotor B		
Turbine Speed (rpm)	**VTG Vanes Angle (deg)**	**Average Tangential Velocity (m/s)**	**Turbine Speed (rpm)**	**VTG Vanes Angle (deg)**	**Average Tangential Velocity (m/s)**
60,000	40	116.90	60,000	40	105.92
	30	132.98		30	109.31
	20	141.19		20	114.77
50,000	40	82.82	50,000	40	74.45
	30	88.22		30	73.17
	20	93.94		20	79.03
40,000	40	27.11	40,000	40	15.91
	30	34.15		30	21.86
	20	48.57		20	27.32

The velocity streamlines at the outlet from the first-stage rotor at the extreme cases are shown in Figure 29.

Figure 29 shows the velocity streamlines of the first-stage rotor at the four extreme cases, which indicated the lowest and highest values of tangential velocity for both rotor geometries. A highly tangential flow of the exhaust gases was observed for the 60,000 rpm, 40° VTG case for both rotors. However, the tangential component was significantly reduced in the 40,000 rpm, 40° VTG case for each rotor geometry. The flow at the first-stage rotor outlet was very chaotic; thus, the configuration of the velocity streamlines shown in Figure 29 might deviate from the parameters presented in Table 12 as those values were area-averaged over the rotor outlet surface.

The variation of the absolute tangential velocity at the outlet from the second-stage rotor is shown in Figure 30.

From Figure 30, one can see that the absolute tangential velocity at the second-stage rotor outlet oscillated within a narrow range of values. The variation pattern of the tangential velocities was different compared to the first-stage rotor velocities shown in Figure 28. The tangential velocity increased with the decrease in the turbine speed, which was associated with the lower expansion capability of the turbine at a low speed. Thus, the outlet exhaust gases contained a vital tangential component which resulted in non-uniform flow. The closed VTG position resulted in a reduced value of the tangential component. Such occurrence improved the flow non-uniformity and reduced the pressure losses at the turbine outlet. The rotor B geometry provided lower tangential velocity for every turbine

speed. The average tangential velocity values are presented in Table 13. In addition, the absolute tangential velocity streamlines are shown in Figure 31.

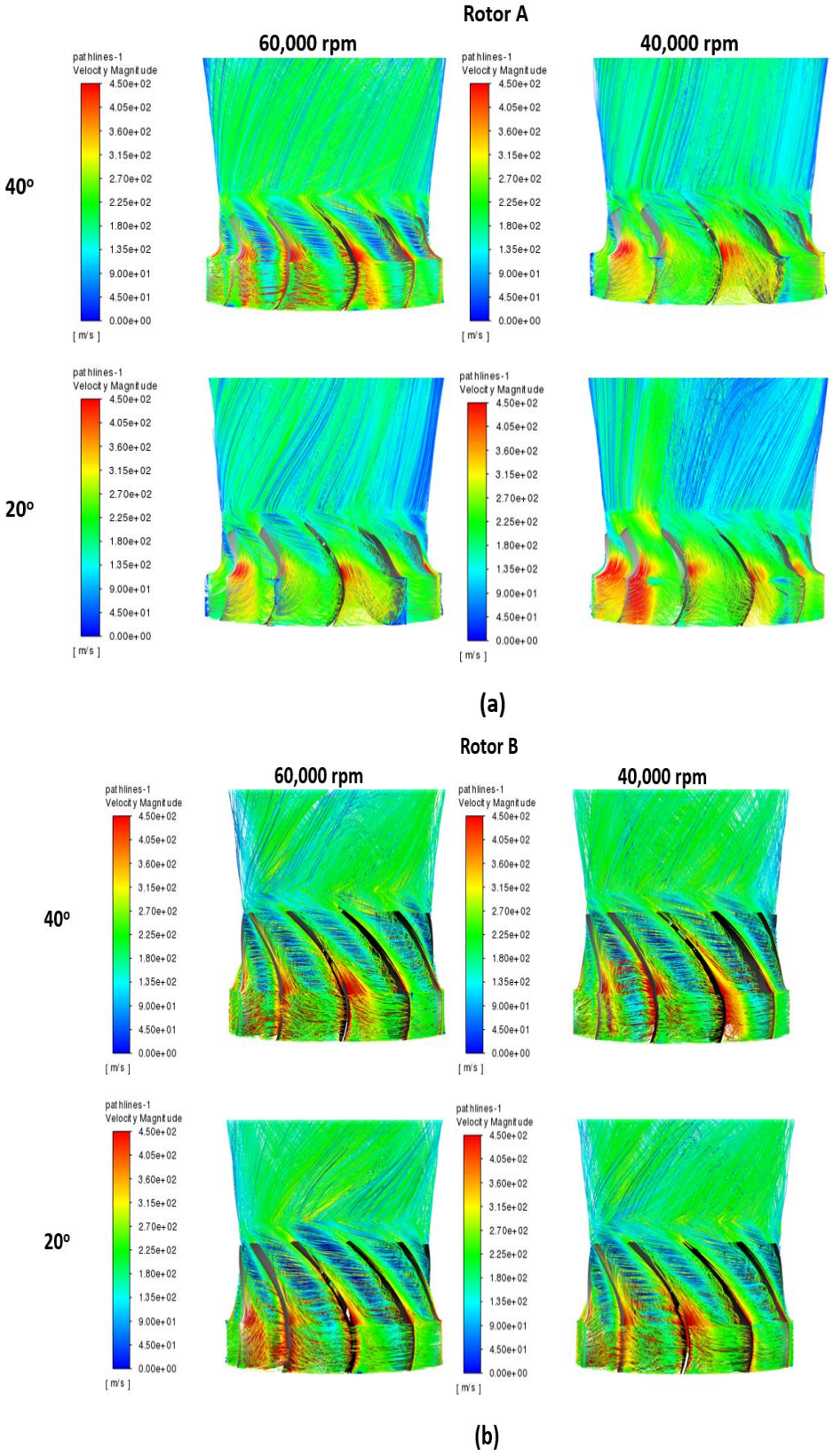

Figure 29. The velocity streamlines at the outlet from the first-stage rotor at two different turbine speeds and VTG positions for: (**a**) rotor A and (**b**) rotor B geometry.

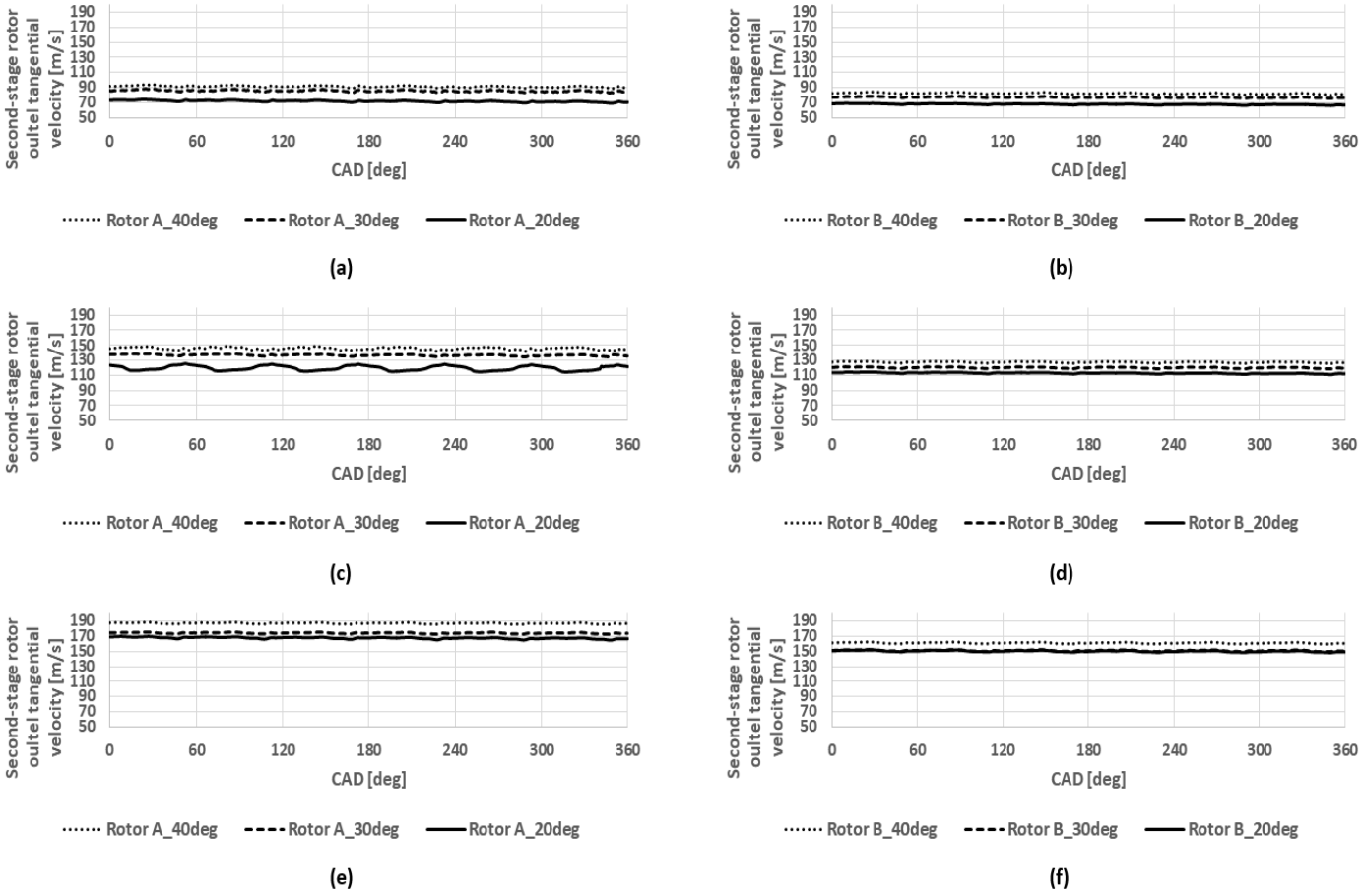

Figure 30. The area-averaged tangential velocity at the outlet from the second-stage rotor: (**a**) rotor A at 60,000 rpm, (**b**) rotor B at 60,000 rpm, (**c**) rotor A at 50,000 rpm, (**d**) rotor B at 50,000 rpm, (**e**) rotor A at 40,000 rpm, (**f**) rotor B at 40,000 rpm.

Table 13. The average values of the second-stage rotor outlet absolute tangential velocity at different turbine speed and VTG vane positions.

Rotor A			Rotor B		
Turbine Speed (rpm)	**VTG Vanes Angle (deg)**	**Average Tangential Velocity (m/s)**	**Turbine Speed (rpm)**	**VTG Vanes Angle (deg)**	**Average Tangential Velocity (m/s)**
60,000	40	91.11	60,000	40	81.71
	30	85.29		30	76.50
	20	71.78		20	67.67
50,000	40	145.88	50,000	40	127.74
	30	137.62		30	119.58
	20	119.68		20	113.00
40,000	40	187.25	40,000	40	161.13
	30	174.32		30	150.84
	20	168.04		20	150.51

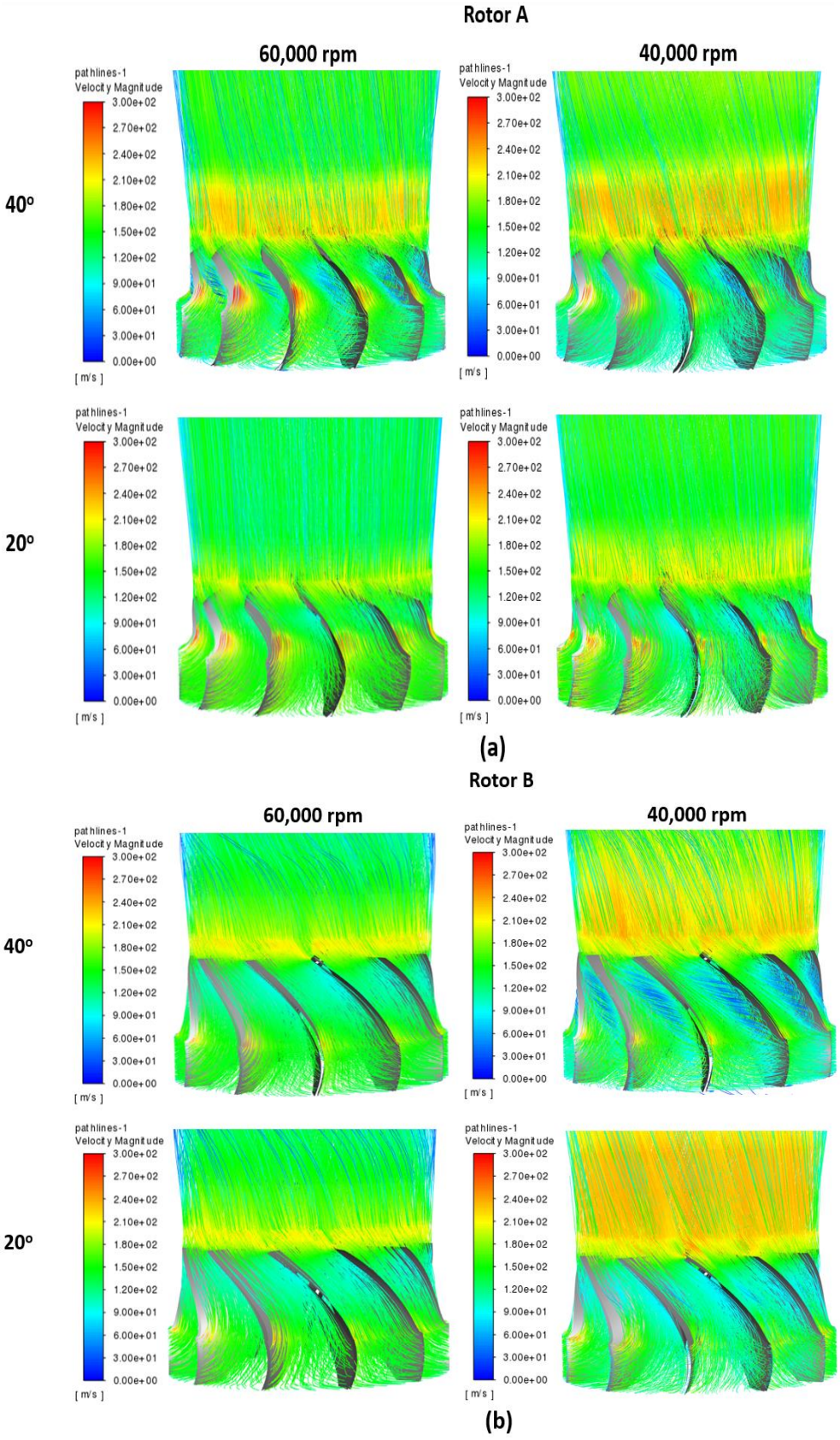

Figure 31. The velocity streamlines at the outlet from the second-stage rotor at two different turbine speeds and VTG positions for: (**a**) rotor A and (**b**) rotor B geometry.

The table shows that rotor B geometry's tangential velocity values were slightly lower than the values for rotor A. The blade geometry of rotor B had a lower forward sweep of the trailing edge compared to rotor A, as seen in Figure 3c,d. Such a blade configuration reduced the generation of the tangential component, especially at the high turbine speed.

The velocity streamlines were shown for four extreme cases at the 60,000 rpm and 40,000 rpm turbine speed with 40° and 20° VTG positions. Such cases provided the highest and lowest values of tangential velocities at the second-stage rotor. One can see that for rotor A geometry, at the 60,000 rpm and 40° VTG position, the velocity streamlines were more deviated from the axial direction than at the 40,000 rpm and 20° VTG position. The same situation was observed for the rotor B geometry at the same conditions. Some disagreements might be found between the area-averaged values in Table 13 and the configuration of the streamlines shown in Figure 31, as the flow at the rotor outlet was very chaotic.

5.6. The Isentropic Efficiency of the First-Stage and Second-Stage Rotor

The expansion capabilities of the first-stage and second-stage rotors were judged based on the averaged isentropic efficiency calculated as:

$$\eta_{iz_{1,2}} = \frac{h_{\mathrm{iz}_{1,3}} - h_{\mathrm{iz}_{2,4}}}{h_{\mathrm{iz}_{1,3}} - h_{2,4}}, \tag{16}$$

where the η_{iz} was the isentropic efficiency. The h_{iz} was the isentropic enthalpy. The indexes "1" and "3" were defined as the inlets to the first- and second-stage rotors. The indexes "2" and "4" were defined as the outlets from the first- and second-stage rotors. The h defined the enthalpy value at the inlet or outlet. The efficiency of the first-stage rotor is shown in Figure 32.

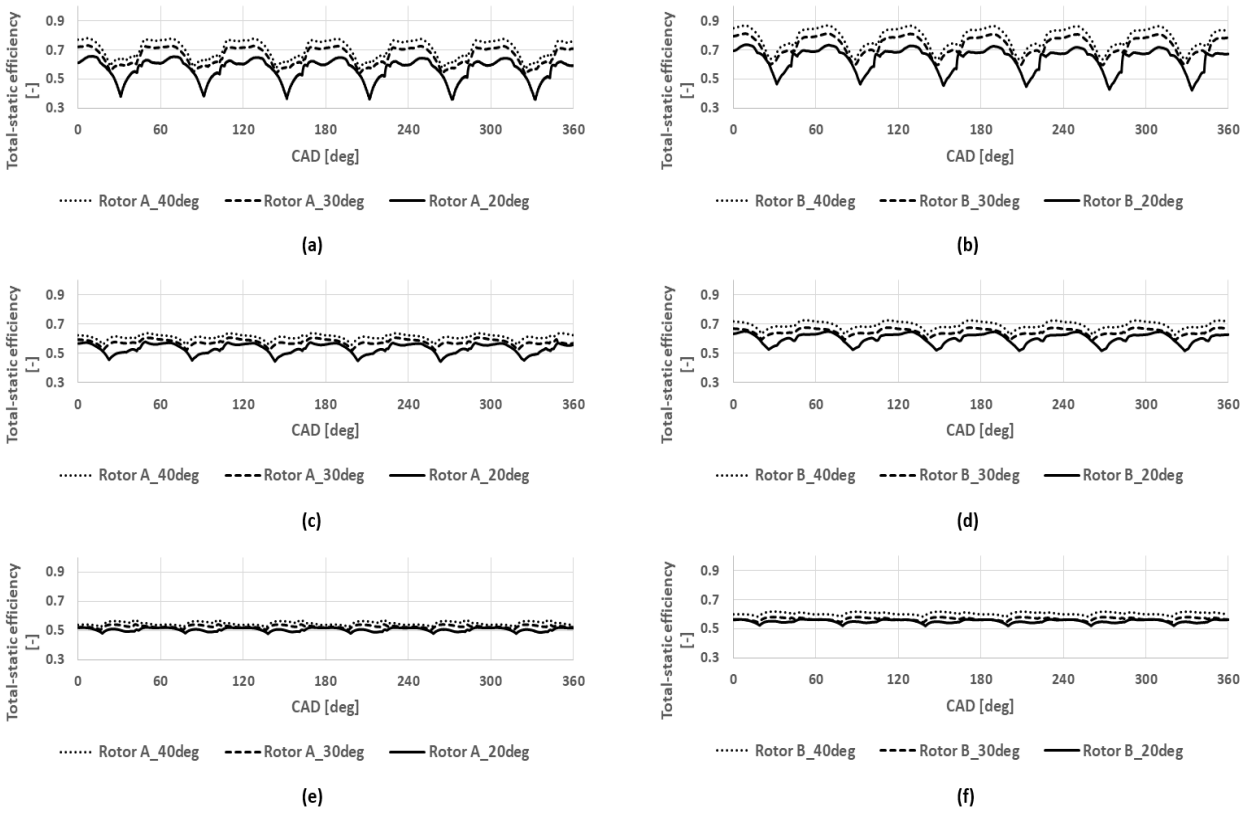

Figure 32. The total-static efficiency changes of the first-stage rotor for two rotor geometries at three different turbine speeds and VTG positions: (**a**) rotor A at 60,000 rpm, (**b**) rotor B at 60,000 rpm, (**c**) rotor A at 50,000 rpm, (**d**) rotor B at 50,000 rpm, (**e**) rotor A at 40,000 rpm, (**f**) rotor B at 40,000 rpm.

Figure 32 shows the first-stage rotor isentropic efficiency for two rotor geometries at different turbine speeds and VTG positions. A strong negative influence of the turbine speed decrease was observed for each rotor geometry. From 60,000 rpm to 40,000 rpm, the efficiency dropped by 29%, significantly decreasing turbine performance. Furthermore, a decrease in turbine performance was observed with the closure of the VTG positions for each rotor geometry. The most significant effect of the VTG closure was observed at the 60,000 rpm speed, as the efficiency decreased by 25% between 40° VTG position and 20° VTG position. The highest efficiency fluctuation was observed at the 60,000 rpm speed, as the velocity of the exhaust gases was the highest in this case. The rotor B geometry provided higher expansion capabilities than rotor A, as its average efficiency was higher by 11.2% at the 60,000 rpm and 50,000 rpm cases. However, these differences were reduced to 7% at the 40,000 rpm case, due to the lower velocity of the exhaust gases. The average values of the isentropic efficiencies for each rotor geometry are shown in Table 14.

Table 14. The average total-static efficiency values of the first-stage rotor for two different rotor geometries.

Rotor A			Rotor B		
Turbine Speed (rpm)	**VTG Vanes Angle (deg)**	**Average Total-Static Efficiency (-)**	**Turbine Speed (rpm)**	**VTG Vanes Angle (deg)**	**Average Total-Static Efficiency (-)**
60,000	40	0.71	60,000	40	0.78
	30	0.66		30	0.73
	20	0.57		20	0.64
50,000	40	0.61	50,000	40	0.69
	30	0.58		30	0.65
	20	0.53		20	0.60
40,000	40	0.55	40,000	40	0.61
	30	0.53		30	0.57
	20	0.51		20	0.55

The total-static efficiency values of the second-stage rotor are shown in Figure 33.

Figure 33 shows the second-stage rotor efficiency changes for two different geometries. In terms of turbine speed, the efficiency of each rotor geometry followed the same trend as the efficiency of the first-stage rotor shown in Figure 32. Both rotors operated more efficiently at higher turbine speeds. However, the efficiency increased significantly with the closure of the VTG vanes. The most substantial influence of the VTG vanes was observed at the 40,000 rpm speed for each rotor geometry. At this speed, the highest difference between the 40° VTG and 20° VTG cases was 45% due to the low velocity of the exhaust gases, which resulted in the high effectiveness of the VTG vanes. However, the highest efficiency of the second-stage rotor was observed at the 60,000 rpm, 20° VTG case for rotors A and B. The efficiency of the rotor B geometry was higher by about 11.2%, which provided a higher performance of the second-stage rotor. This difference was caused by the lower flow losses inside the rotor passages, as shown in another section of this paper. The average efficiency values of the second-stage rotor are shown in Table 15.

By comparing efficiency values in Tables 14 and 15, one can see that the efficiency of the second-stage rotor was higher than that of the first-stage rotor. The position of the first-stage rotor in the upstream direction from the VTG vanes increased the exhaust gases' backpressure, which negatively affected the turbine performance. The increased backpressure led to the pressure increase at the outlet of the first-stage rotor, which limited its pressure ratio. On the other hand, the second-stage rotor was not affected by the backpressure due to its downstream position from the VTG vanes. Moreover, the changes in the VTG vanes' positions led to an increase in rotor efficiency.

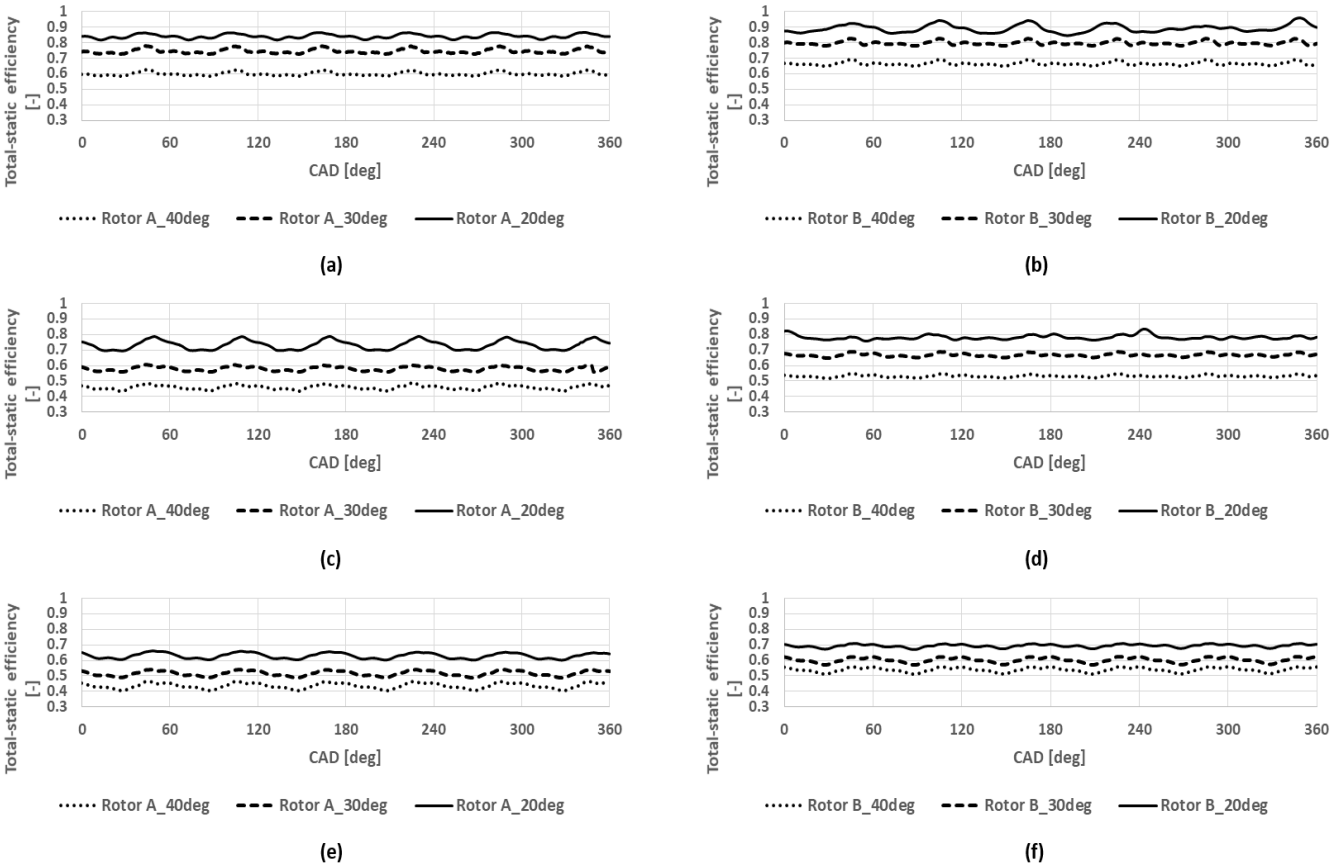

Figure 33. The changes of the second-stage rotor efficiency with two different rotor geometries at three different turbine speeds and VTG positions: (**a**) rotor A at 60,000 rpm, (**b**) rotor B at 60,000 rpm, (**c**) rotor A at 50,000 rpm, (**d**) rotor B at 50,000 rpm, (**e**) rotor A at 40,000 rpm, (**f**) rotor B at 40,000 rpm.

Table 15. The average total-static efficiency values of the second-stage rotor for two different rotor geometries.

Rotor A			Rotor B		
Turbine Speed (rpm)	**VTG Vanes Angle (deg)**	**Average Total-Static Efficiency (-)**	**Turbine Speed (rpm)**	**VTG Vanes Angle (deg)**	**Average Total-Static Efficiency (-)**
60,000	40	0.60	60,000	40	0.66
	30	0.75		30	0.80
	20	0.84		20	0.89
50,000	40	0.46	50,000	40	0.53
	30	0.58		30	0.67
	20	0.73		20	0.78
40,000	40	0.43	40,000	40	0.47
	30	0.52		30	0.60
	20	0.63		20	0.69

5.7. The Flow Losses at the First-Stage and Second-Stage Rotor

The authors analyzed the exhaust gas flow losses through the rotor passage at the first and second stages. Two reference points were chosen for the comparison, as shown in Figure 34.

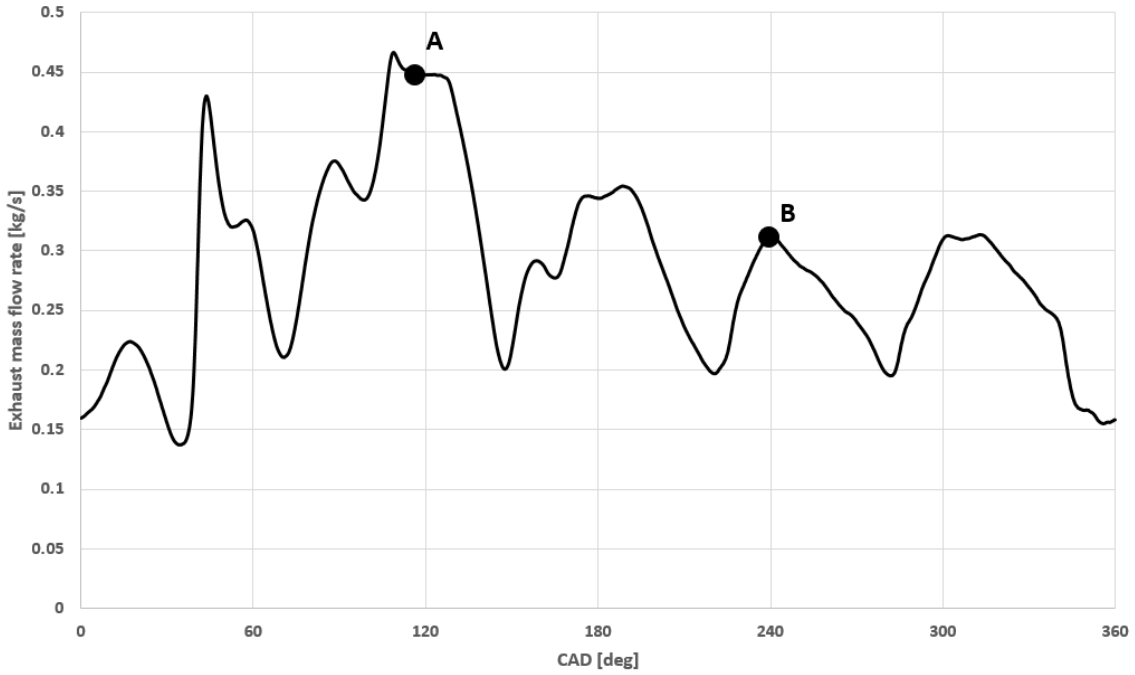

Figure 34. The mass-flow rate changes at the exhaust pipe with reference point A (peak mass flow rate) and B (low mass flow rate).

The reference points were chosen based on the exhaust pipe mass-flow rate changes during the single revolution of the crankshaft. Reference point A represented the peak mass-flow rate value after the opening of the exhaust valve. In contrast, point B represented the lowest value of the mass-flow rate after the closure of the exhaust valve. The analysis was performed at the blade pressure side for each rotor geometry. The phase shift was included during the simulation to account for the time delay between two rotor stages. Two extreme turbine speeds and VTG positions were chosen for the comparison: 60,000 rpm, 40,000 rpm, 40° VTG, and 20° VTG cases. The results of the first-stage rotor analysis are shown in Figure 35.

Figure 35 shows the velocity streamlines at the pressure side of the first-stage rotor blade for two rotor geometries. Figure 35a shows the results at 60,000 rpm speed, while Figure 35b shows the results at 40,000 rpm speed. The left column of Figure 35 shows the velocity streamline changes of the rotor A geometry. The left side shows the velocity streamline changes of the rotor B geometry. The streamlines were shown during A and B reference points for each VTG position. Firstly, by comparing the velocity streamlines in Figure 35a,b, one can see that the velocity on the blade pressure surface was lower at the 40,000 rpm speed for each case. For rotor A geometry, the secondary-flow structures were observed near the rotor hub, close to the turbine inlet.

Such structures were the most evident at the 40,000 rpm speed. Such observation corresponded with the low efficiency of the first-stage rotor A, shown in Figure 32. Moreover, the secondary-flow structures were more evident at the 20° VTG position for rotor A geometry as the backpressure increased with the closure of the VTG vanes. Such a phenomenon led to decreased rotor performance, which was observed in the efficiency decrease shown in Figure 32a,c,e. The separation areas were presented at both A and B reference points. However, such large flow structures were not observed for the rotor B geometry. At the 60,000 rpm speed, rotor B provided a higher velocity of the exhaust gases through the passage without a significant separation area. However, at 40,000 rpm, minor separation areas were presented near the rotor hub. In addition, the exhaust gas velocity through the rotor at this speed seemed lower than in the 60,000 rpm case, leading to the efficiency decrease. The lack of significant secondary-flow structures led to the higher efficiency values of the rotor B geometry at the first stage, as shown in Table 14.

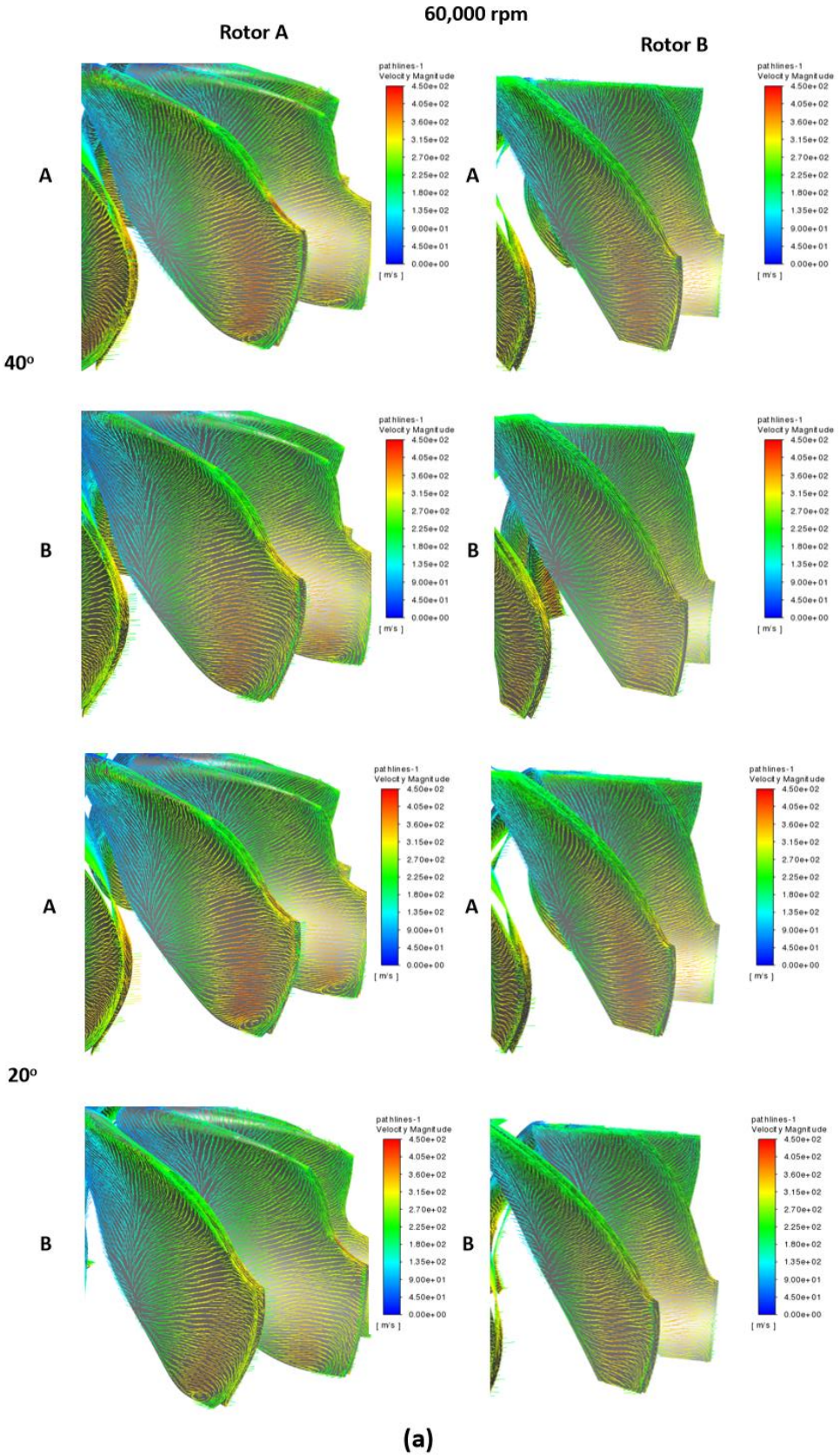

Figure 35. *Cont*.

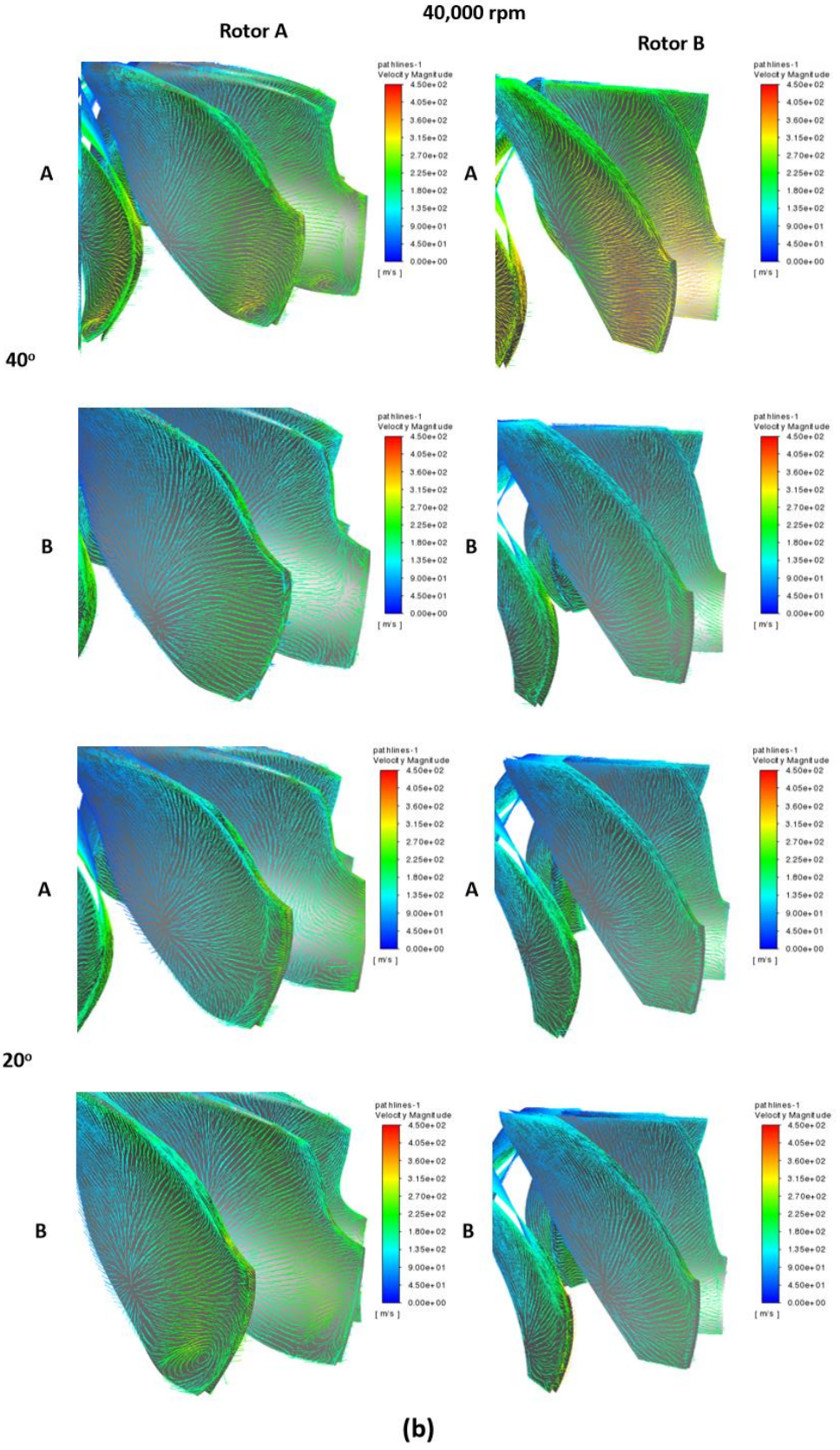

Figure 35. The first-stage rotor velocity streamlines for two different rotor geometries, VTG positions, A and B operating conditions and at the (**a**) 60,000 rpm and (**b**) 40,000 rpm turbine speed.

The velocity streamlines of the second-stage rotor are shown in Figure 36.

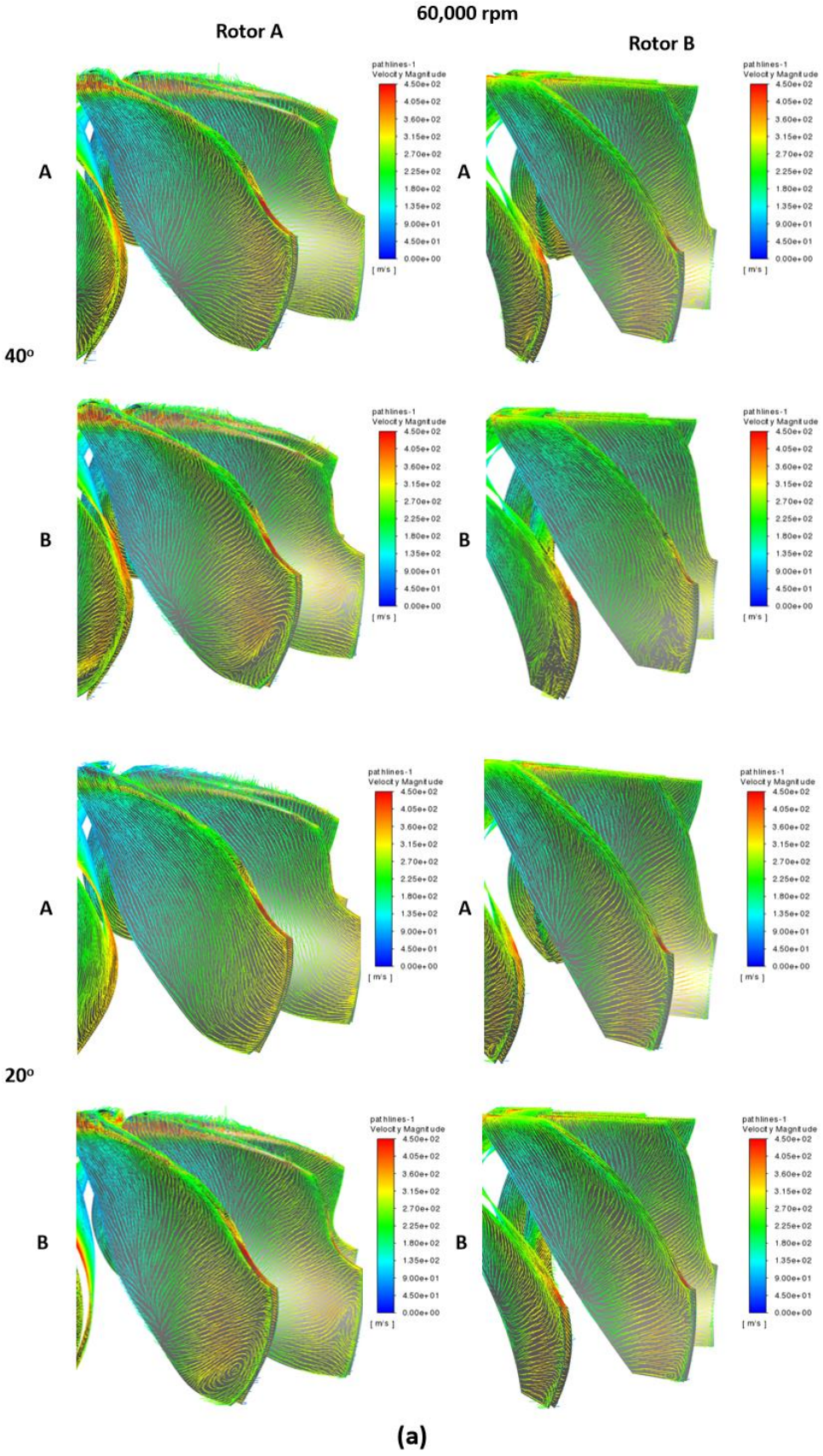

Figure 36. *Cont*.

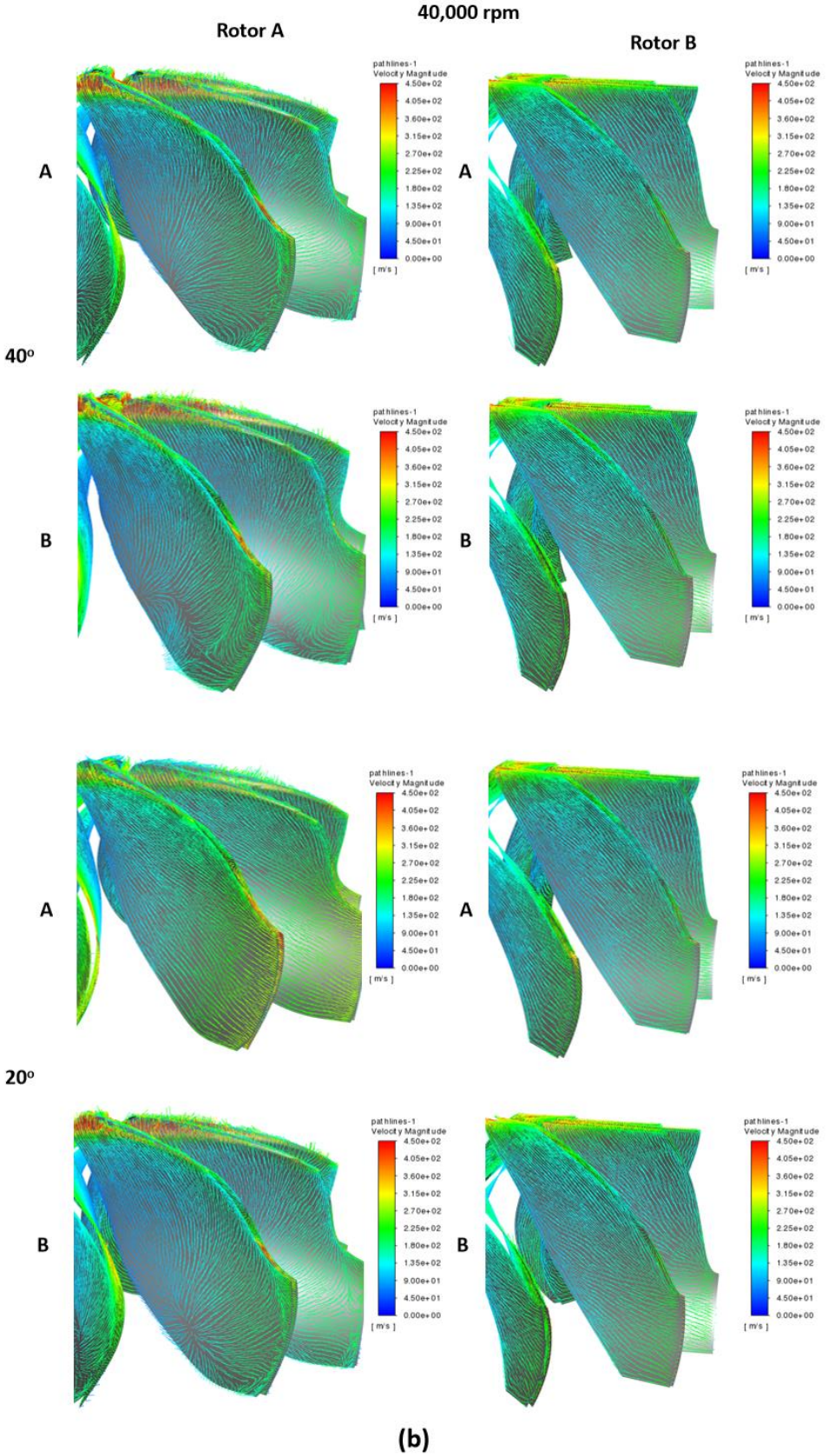

Figure 36. The second-stage rotor velocity streamlines for two different rotor geometries, VTG positions, A and B operating conditions and at the (**a**) 60,000 rpm and (**b**) 40,000 rpm turbine speed.

The configuration of Figure 36 is identical to Figure 35. For the rotor A geometry, the secondary-flow structures were mainly observed at the low value of the exhaust mass-flow rate indicated as reference point B. At reference point B, the separation structures were observed near the rotor hub and the rotor inlet's whole span. The most evident flow losses were presented through the blade span near the inlet at reference point B, at 40,000 rpm speed and 40° VTG position. These observations were supported by the low rotor efficiency values shown in Figure 33e. Almost no separation points were observed at reference point A, which was favorable regarding rotor efficiency. For the rotor B geometry, almost no separation structures were presented. A significant separation was observed at reference point B at 60,000 rpm speed and 40° VTG position, which might have been caused by the high ratio of the blade tip velocity to the exhaust gases velocity. At 60,000 rpm, the rotor passage's velocity values were higher than those shown at 40,000 rpm for the rotor B geometry. The absence of the secondary-flow structures of the rotor B geometry led to a significant increase in the rotor efficiency for each test case, as shown in Tables 14 and 15.

The extensive numerical simulation of the two-stage turbine system for two different rotor geometries provided insight into each geometry's performance at every turbine stage. Despite being only virtually scaled up to match rotor A, the state-of-the-art rotor B provided higher expansion capabilities than available rotor A. Rotor B provided higher performance at every turbine speed and VTG position than rotor A. The highest total efficiency value of the rotor B two-stage turbine was 57%, obtained for the 60,000 rpm, 20° VTG case.

The presented waste heat recovery system is unique as it consists of two turbine stages on the same shaft. There were only a few approaches to deal with the problem of flow separation or unequal admission. The first approach was a MEDUSA (Multiple Exhaust Duct with Source Adjustment) project which replaced the traditional volute with multi-channel casing to provide flow controllability to the radial inflow turbine [22]. The multi-channel casing consisted of four inlets placed circumferentially around the turbine. The steady-state CFD model was optimized to meet the highest efficiency and pressure-ratio values. The mass flow of exhaust gases was intended to be controlled by the externally-installed valves. The steady-state calculations showed that the flow disturbances cause the turbine efficiency to decrease, especially at the partial admission configuration [33]. Another approach dealt with the single-stage axial turbine with the six-inlet case configuration under pulse flow conditions [34]. Such a daring configuration was simulated and tested by the authors. An axial turbine provided a relatively simple connection between the exhaust pipes and turbine casing. It should also be noted that due to the greater diameter of the axial turbine, the turbine inlet area from each exhaust pipe could be significantly increased which in turn could provide higher values of the exhaust flow.

On the other hand, axial turbines operate under lower speed values than radial turbines due to their larger diameter, which could provide lower heat recovery capability. Moreover, the radial turbines operate more efficiently under off-design conditions. It is worth mentioning that the two-stage system not only enhances the waste heat recovery thanks to two rotors, but also provides high efficiency at different engine working conditions due to the second-stage VTG nozzle.

6. Conclusions

In this paper, the numerical simulations of the two-stage turbine system were investigated. The numerical model consisted of the unique turbine inlet domain, the first-stage nozzle vanes domain, the rotor gap domain, the first-stage rotor domain, the diffuser do-main, the inter-stage pipes domain, the VTG vanes domain, the second-stage rotor do-main, and the outlet domain. Both the first- and second-stage rotors were generated from the same rotor geometry.

The two types of rotor geometries chosen for comparison were the older rotor version (rotor A) and the state-of-the-art rotor geometry (rotor B). The actual geometry of rotor B had a smaller inlet diameter than rotor A. Thus, to make a fair comparison of both geometries, rotor B was scaled up to match the dimensions of rotor A. Authors performed

the geometrical comparison of the rotor geometries with the angular comparison of theta and beta angles.

The geometry of both rotors was generated using the 3-D scanner. The numerical domain and the numerical mesh were made using ANSYS ICEM CFD software.

The transient simulations with the sliding mesh approach were performed for rotor A and rotor B geometries at three turbine speeds (60,000 rpm, 50,000 rpm and 40,000 rpm), and three VTG positions (40°, 30°, and 20°). The mass-flow rate boundary conditions were set at the inlet to each exhaust pipe and obtained from the six-cylinder engine's experimental test stand.

The simulation convergence condition was met at the ninth revolution of the crankshaft and the validation was performed based on the number of numerical elements and the RMSE error.

The leakage between adjacent exhaust pipes was investigated regarding the mass flow rate of exhaust gases through the rotor gap domain. It was found the exhaust flow though the gap greatly depends on the opening and closure events of the exhaust valves. On the other hand, turbine speed and the VTG position had minor influence on the exhaust mass flow changes through the gap. However, it was found that only 10% of the total exhaust mass flow was leaked through the rotor gap, which provides a positive aspect of the pulse separation feature of the inlet hub.

The pressure and temperature changes at the inlet and outlet of the first-stage rotor and second-stage rotor were significantly affected by the closure of the VTG vanes. It was evident that at the first-stage rotor and 20° VTG position, the pressure and temperature rise was notable due to increased backpressure. The closure of the VTG vanes led to increased outlet pressure at the first-stage rotor, which limited its pressure ratio. On the other hand, the second-stage rotor provided higher pressure ratio values and lower outlet temperature values for both rotor geometries. In addition, the closure of the VTG had a positive effect on the pressure-ratio increase and the decrease in the outlet temperature of the second-stage rotor. However, the outlet temperature decrease was minor compared to the pressure-ratio increase. The performance of the first- and second-stage rotors decreased with the decrease in the turbine speed, which was observed in both pressure and temperature changes.

The rotor B geometry provided a higher performance of the first- and second-stage rotors. The higher pressure ratio and lower outlet temperature for the first-stage rotor B was achieved due to the smaller blade number than rotor A. Thus, rotor B was less affected by the closure of the VTG vanes. The rotor B geometry at the second stage provided higher pressure ratio values and lower outlet temperature values than rotor A at each turbine speed. The highest temperature drop difference between rotors A and B was 11% at the first-stage rotor and 58% at the second-stage rotor. The authors concluded that the state-of-the-art rotor B, with the exact same dimensions as rotor A, could provide higher performance than the older rotor A.

The analysis of the tangential velocity component at the outlet from the first- and second-stage rotors showed an increased turbulent flow. The closure of the VTG vanes increased the tangential velocity at the first-stage rotor outlet, which resulted in high flow deviation of the exhaust gases from the axial direction. However, the opposite behavior was observed at the second-stage rotor, as the closure of VTG vanes promoted axial flow of the exhaust gases. Rotor B provided lower values of the tangential velocity for every stage, which led to the less turbulent flow than in the case of the rotor A geometry.

The comparison of the isentropic efficiency of the first- and second-stage rotors provided insight into the heat recovery possibilities of each rotor geometry. The negative influence of the VTG vanes on the first-stage rotor provided lower efficiency values, especially at the low turbine speed. The highest efficiency values of the first-stage rotor were achieved at the 60,000 rpm, 40° VTG case where the flow resistance was the lowest. However, at the high turbine speed, significant efficiency changes were observed due to the high velocity of exhaust gases. Such efficiency changes were reduced at the low turbine speed.

On the other hand, the second-stage rotor enhanced heat recovery with the closure of the VTG vanes. The highest efficiency values of the second-stage rotor were observed at the 60,000 rpm, 20° VTG case for every rotor geometry. The highest flow losses were observed at the blade hub region near the rotor inlet for the rotor A geometry at both stages. For the first-stage rotor A, the flow separation was more evident at the closed position of the VTG vanes. At the second-stage rotor A, the separation area was evident at the opened position of the VTG vanes. However, almost no separation zones were observed for the rotor B blade geometry at each stage. Thus, the rotor B geometry provided the highest total efficiency of the two-stage turbine system with the value of 57%.

The authors performed the simulations of the promising and unique two-stage turbine system model, which provided a significant leakage reduction of the exhaust gases between the adjacent exhaust pipes. The simplicity of such a system provided an alternative to the complicated turbocharging systems, especially for multi-cylinder engines which require a turbocharging system that properly separates the exhaust pulses according to the engine firing order. The most well-known turbocharging systems used in multi-cylinder engines are twin-turbo and bi-turbo turbocharging, requiring two turbochargers on a single engine. Such systems require a large amount of space, which increases engine weight and, thus, fuel consumption. In addition, such systems require a very complex pipeline system which should be connected to each turbocharger to avoid interference of the exhaust pulses. The two-stage turbine system might compete with those systems in terms of space reduction and the simplicity of the pipeline system. Moreover, such a system is innovative in terms of exhaust heat recovery compared to the other proposed systems, as it employs two rotors on a single shaft. The first-stage rotor acts as an exhaust pulse separator and the second one acts as the actual heat recovery device. However, both rotors provide recovery of the heat energy from the exhaust gases. The implementation of the VTG system might also further increase engine performance, especially at low engine speed or for the aviation industry at high altitude flights.

Author Contributions: Conceptualization, D.K. and P.M.; methodology, D.K. and P.M.; resources, D.K.; writing, D.K.; supervision, P.M. All authors have read and agreed to the published version of the manuscript.

Funding: This work is a part of the Applied Research Programme of the National Centre for Research and Development within the scope of applied research in industry branches (programme path B) „Badania wysokosprawnego silnika wykorzystującego technologię HCCI do zastosowań w energetyce rozproszonej" (GENEKO)—contract number PBS3/B4/16/2015.

Data Availability Statement: Not applicable.

Acknowledgments: The authors are pleased to acknowledge BorgWarner Poland company for their support in research.

Conflicts of Interest: The authors declare no conflict of interest.

Nomenclature

Notations

w	Relative velocity
c	Absolute velocity
u	Linear velocity
h^*	Total enthalpy
η	Turbine total-static efficiency
X	Measured/observed value
n	Number of measurements
π_T	Turbine pressure-ratio
p	Pressure
h	Static enthalpy
k'	Heat capacity ratio of exhaust gases

R'	Gas constant of exhaust gases
T^*	Total temperature
ρ	Density
t	Time
U	Vector of velocity
τ	Molecular stress tensor
S_M	Momentum source
λ	Thermal conductivity
T	Static temperature
S_E	Energy source
x_j	Position vector in tensor rotation
$\check{\nu}$	Modified turbulent kinematic viscosity
G_v	Production of turbulent viscosity
$G_{\check{\nu}}$	S-A turbulence model constant
G_{b2}	S-A turbulence model constant
Y_v	Destruction of turbulent viscosity
$S_{\check{\nu}}$	Source term
f_{v1}	Damping function
Abbreviations	
ICE	Internal combustion engine
3-D	Three-dimensional
1-D	One-dimensional
LE	Leading edge
TE	Trailing edge
CAD	Crank angle degree
CFD	Computational fluid dynamics
VTG	Variable Turbine Geometry
RMSE	Root mean square error
St	Strouhal number
Subscripts	
0	Conditions at the rotor inlet
1	Conditions after first-stage nozzle vanes
2	Conditions after first-stage rotor
3	Conditions before second-stage rotor
4	Conditions after second-stage rotor
tot	Total

References

1. Nikita, C. Pulsating Flow Phenomena in Exhaust Manifolds. Ph.D. Thesis, Imperial College, London, UK, August 2017.
2. Gopal, P.; Kumar, T.S.; Kumaragurubaran, B. Analysis of Flow through the Exhaust Manifold of a Multi Cylinder Petrol Engine for Improved Volumetric Efficiency. *Int. J. Dyn. Fluids* **2009**, *5*, 15.
3. Poal, D.; Dwyer, M. A Simple Theory for Pressure Pulses in Exhaust Systems. *Proc. Inst. Mech. Eng.* **1964**, *179*, 365–394. [CrossRef]
4. Semlitsch, B.; Wang, Y.; Mihăescu, M. Flow Effects due to Pulsation in an Internal Combustion Engine Exhaust Port. *Energy Convers. Manag.* **2014**, *86*, 520–536. [CrossRef]
5. Hong, B.; Venkataraman, V.; Cronhjort, A. Numerical Analysis of Engine Exhaust Flow Parameters for Resolving Pre-Turbine Pulsating Flow Enthalpy and Exergy. *Energies* **2021**, *14*, 6183. [CrossRef]
6. Serrano, J.; Arnau, F.; Gracía, L.; Samala, V.; Smith, L. Experimental Approach for the Characterization and Performance Analysis of Twin Entry Radial-Inflow Turbines in a Gas Stand and with Different Flow Admission Conditions. *Appl. Therm. Eng.* **2019**, *159*, 113737. [CrossRef]
7. Usai, V.; Marelli, S. Steady State Experimental Characterization of a Twin Entry Turbine under Different Admission Conditions. *Energies* **2021**, *14*, 2228. [CrossRef]
8. Copeland, D.; Martinez-Botas, R.; Seiler, M. Comparison Between Steady and Unsteady Double-Entry Turbine Performance Using the Quasi-Steady Assumption. *ASME J. Turbomach.* **2011**, *133*, 031001. [CrossRef]
9. Marelli, S.; Capobianco, M. Steady and Pulsating Flow Efficiency of a Waste-Gated Turbocharger Radial Flow Turbine for Automotive Application. *Energy* **2011**, *36*, 459–465. [CrossRef]
10. Chiong, M.; Rajoo, S.; Romagnoli, A.; Costall, A.; Martinez-Botas, R. One-Dimensional Pulse-Flow Modeling of a Twin-Scroll Turbine. *Energy* **2016**, *115*, 1291–1304. [CrossRef]

11. Chen, H.; Hakeem, I.; Martinez-Botas, R. Modelling of a Turbocharger Turbine Under Pulsating Inlet Conditions. *Proc. Inst. Mech. Eng. Part A J. Power Energy* **1996**, *210*, 397–408. [CrossRef]
12. Yang, M.; Deng, K.; Martines-Botas, R.; Zhuge, W. An Investigation on Unsteadiness of a Mixed-Flow Turbine Under Pulsating Conditions. *Energy Convers. Manag.* **2016**, *110*, 51–58. [CrossRef]
13. Chiong, M.; Rajoo, S.; Romagnoli, A.; Costall, A.; Martinez-Botas, R. Non-Adiabatic Pressure Loss Boundary Condition for Modelling Turbocharger Turbine Pulsating Flow. *Energy Convers. Manag.* **2015**, *93*, 267–281. [CrossRef]
14. Wang, H.; Chao, Y.; Tang, T.; Luo, K.; Qin, K. A Comparison of Partial Admission Axial and Radial Inflow Turbines for Underwater Vehicles. *Energies* **2021**, *14*, 1514. [CrossRef]
15. Newton, P.; Copeland, C.; Martinez-Botas, R.; Seiler, M. An Audit of Aerodynamic Loss in a Double Entry Turbine under Full and Partial Admission. *Int. J. Heat Fluid Flow* **2012**, *33*, 70–80. [CrossRef]
16. Copeland, C.; Newton, P.; Martinez-Botas, R.; Seiler, M. A Comparison of Timescales within a Pulsed Flow Turbocharger Turbine. In Proceedings of the Institution of Mechanical Engineers—10th International Conference on Turbochargers and Turbocharging, London, UK, 15–16 May 2012.
17. Yang, B.; Martinez-Botas, R.; Yang, M. Rotor Flow-Field Timescale and Unsteady Effects on Pulsed-Flow Turbocharger Turbine. *Aerosp. Sci. Technol.* **2022**, *120*, 107231. [CrossRef]
18. Xue, Y.; Yang, M.; Martinez-Botas, R.; Yang, B.; Deng, K. Unsteady Performance of a Mixed-Flow Turbine with Nozzled Twin-Entry Volute Confronted by Pulsating Incoming Flow. *Aerosp. Sci. Technol.* **2019**, *95*, 105485. [CrossRef]
19. Cerdoun, M.; Ghenaiet, A. Unsteady Behavior of a Twin Entry Radial Turbine under Engine Like Inlet Flow Conditions. *Appl. Therm. Eng.* **2018**, *130*, 93–111. [CrossRef]
20. Padzillah, M.; Rajoo, S.; Martinez-Botas, R. Influence of Speed and Frequency towards the Automotive Turbocharger Turbine Performance under Pulsating Flow Conditions. *Energy Convers. Manag.* **2014**, *80*, 416–428. [CrossRef]
21. Fürst, J.; Zak, Z. Numerical Simulation of Unsteady Flows Through a Radial Turbine. *Adv. Comput. Math.* **2019**, *45*, 1939–1952. [CrossRef]
22. Hassan, A.; Fuhrer, C.; Schatz, M.; Vogt, D. Multi-channel Casing Design for Radial Turbine Operation Control. In Proceedings of the 13th European Conference on Turbomachinery Fluid Dynamics & Thermodynamics ETC13, Lausanne, Switzerland, 8–12 April 2019. [CrossRef]
23. Zhao, R.; Li, W.; Zhuge, W.; Zhang, Y. Unsteady Flow Loss Mechanism and Aerodynamic Improvement of Two-Stage Turbine under Pulsating Conditions. *Entropy* **2019**, *21*, 985. [CrossRef]
24. BorgWarner Performance Turbochargers Catalog. Available online: https://images.carid.com/borgwarner/info/pdf/airwerks-intro.pdf (accessed on 16 November 2022).
25. Zahed, A.; Bayomi, N. Radial Turbine Design Process. *ISESCO J. Sci. Technol.* **2015**, *11*, 9–22.
26. Continuity and Momentum Equations. Available online: https://www.afs.enea.it/project/neptunius/docs/fluent/html/th/node11.htm (accessed on 19 December 2022).
27. Kozak, D.; Mazuro, P.; Teodorczyk, A. Numerical Simulation of Two-Stage Variable Geometry Turbine. *Energies* **2021**, *14*, 5349. [CrossRef]
28. Galindo, J.; Fajardo, P.; Navarro, R.; Garcia-Cuevas, L. Characterization of a Radial Turbocharger Turbine in Pulsating Flow by Means of CFD and its Application to Engine Modeling. *Appl. Energy* **2013**, *103*, 116–127. [CrossRef]
29. Spalart, P.; Allmaras, S. A One-Equation Turbulence Model for Aerodynamic Flows. *Rech. Aerosp.* **1994**, *1*, 5–21. [CrossRef]
30. Zhang, Y.; Chen, L.; Zhuge, W.; Zhang, S. Effects of Pulse Flow and Leading Edge Sweep on Mixed Flow Turbines for Engine Exhaust Heat Recovery. *Sci. China Technol. Sci.* **2011**, *54*, 295–301. [CrossRef]
31. Yang, M.; Martinez-Botas, R.; Rajoo, S.; Yokoyama, T.; Ibaraki, S. An Investigation of Volute Cross-Sectional Shape on Turbocharger Turbine Under Pulsating Conditions in Internal Combustion Engine. *Energy Convers. Manag.* **2015**, *105*, 167–177. [CrossRef]
32. Transport Equation for the Spalart-Allmaras Model. Available online: https://www.afs.enea.it/project/neptunius/docs/fluent/html/th/node50.htm (accessed on 19 December 2022).
33. Hassan, A.; Schatz, M.; Vogt, A. Performance and Losses Analysis for Radial Turbine Featuring a Multi-Channel Casing Design. *J. Turbomach.* **2021**, *143*, 021003. [CrossRef]
34. Anton, N.; Birkestad, P. *The 6-Inlet Single Stage Axial Turbine Concept for Pulse-Turbocharging: A Numerical Investigation*; SAE Technical Paper; SAE: Warrendale, PA, USA, 2019. [CrossRef]